TECTONICS, VOL. 32, 191–215, doi:10.1002/tect.20021, 2013

Orogen-parallel ductile extension and extrusion of the Greater Himalaya in the late Oligocene and Miocene

Zhiqin Xu,[1] Qin Wang,[2] Arnaud Pêcher,[3] Fenghua Liang,[1] Xuexiang Qi,[1] Zhihui Cai,[1] Huaqi Li,[1] Lingsen Zeng,[1] and Hui Cao[1]

Received 2 August 2012; revised 9 January 2013; accepted 3 February 2013; published 29 April 2013.

[1] Predominant stretching structures in the Greater Himalayan Crystalline Complex (GHC) trend perpendicular to the belt and are linked to the southward exhumation or emplacement of the GHC between the South Tibet Detachment (STD) and the Main Central Thrust. However, our field investigations in southern Tibet reveal the widespread presence of gently dipping shear zones with a penetrative orogen-parallel stretching lineation, which separates the Tethyan Himalayan Sequence and the underlying GHC. The shear zones are well preserved in the upper part of the GHC, south to and structurally lower than the STD. Field criteria, microstructures, and quartz fabrics indicate top-to-the-east shearing in the Yadong shear zone (eastern GHC), coexistence of top-to-the-east and top-to-the-west shearing in the Nyalam shear zone (central GHC), but top-to-the-west shearing in the Pulan shear zone (western GHC). Characteristic microstructures and slip systems of quartz in the high-grade GHC rocks resulted from the lateral flow under upper amphibolite (up to 650–700 °C) to greenschist facies conditions. U-Pb ages of metamorphic zircon rims by sensitive high-resolution ion microprobe (SHRIMP) and laser ablation multi-collector inductively coupled plasma mass spectrometry (LA-MC-ICP-MS) analyses yield 28–26 Ma for the initiation of the Yadong and Nyalam shear zones and 22–15 Ma for the activation of the Pulan shear zone. In addition, $^{40}Ar/^{39}Ar$ cooling ages of biotite and muscovite suggest cessation of ductile sharing at 13–11 Ma on the Yadong shear zone, which is coeval with the activation of the STD. Combined with previous studies, we propose that initiation of orogen-parallel extension marks the transition from burial/crustal thickening to exhumation of the GHC. Due to lateral crustal thickness gradients in a thickened crust, orogen-parallel gravitational collapse occurred within the convergent Himalayan orogen in the late Oligocene-Miocene. This tectonic denudation triggered and enhanced partial melting and ductile extrusion of the GHC in the Miocene.

Citation: Xu, Z., Q. Wang, A. Pêcher, F. Liang, X. Qi, Z. Cai, H. Li, L. Zeng, and H. Cao (2013), Orogen-parallel ductile extension and extrusion of the Greater Himalaya in the late Oligocene and Miocene, *Tectonics*, *32*, 191–215, doi:10.1002/tect.20021.

1. Introduction

[2] Bounded by the north-dipping Main Central Thrust (MCT) below and the South Tibet Detachment (STD) above, the Greater Himalayan Crystalline Complex (GHC) forms the metamorphic core of the Himalayan orogen and represents the subducted northern margin of the Indian continent (Figure 1) [e.g., *Le Fort*, 1996; *Yin and Harrison*, 2000; *Yin*, 2006; *Guillot et al*., 2008; *Yin et al*., 2010a; *Webb et al*., 2011a]. In the middle Eocene to Oligocene, the GHC experienced upper amphibolite to granulite facies prograde metamorphism due to subduction (burial/crustal thickening) [e.g., *Searle et al*., 1992; *Hodges et al*., 1994; *Vance and Harris*, 1999; *Ding and Zhong*, 1999; *Zhang et al*., 2010]. Exhumation of the GHC in the context of the Indo-Asian collision is the key issue for understanding the evolution of the Himalayan orogen. The predominant stretching lineation in the GHC trends north to N30°E (orogen perpendicular), which has been attributed to the southward exhumation of these middle crustal rocks between the STD and MCT in wedge extrusion [e.g., *Burchfiel and Royden*, 1985; *Grujic et al*., 1996] and channel flow models [e.g., *Beaumont et al*., 2001; *Hodges et al*., 2001; *Grujic et al*., 2002] or to emplacement of the GHC between the MCT and STD in tectonic wedging models [*Yin*, 2006; *Webb et al*., 2007, 2011a, 2011b].

[1]State Key Laboratory of Continental Tectonics and Dynamics, Institute of Geology, Chinese Academy of Geological Sciences, Beijing, China.
[2]State Key Laboratory for Mineral Deposits Research, Department of Earth Sciences, Nanjing University, Nanjing, China.
[3]ISTerre, Maison des Géosciences, University of Grenoble and CNRS, Grenoble, France.

Corresponding authors: Zhiqin Xu, State Key Laboratory of Continental Tectonics and Dynamics, Institute of Geology, Chinese Academy of Geological Sciences, Beijing 100037, China (xzq@ccsd.cn); Qin Wang, State Key Laboratory for Mineral Deposits Research, Department of Earth Sciences, Nanjing University, Nanjing 210093, China (qwang@nju.edu.cn).

0278-7407/13/10.1002/tect.20021

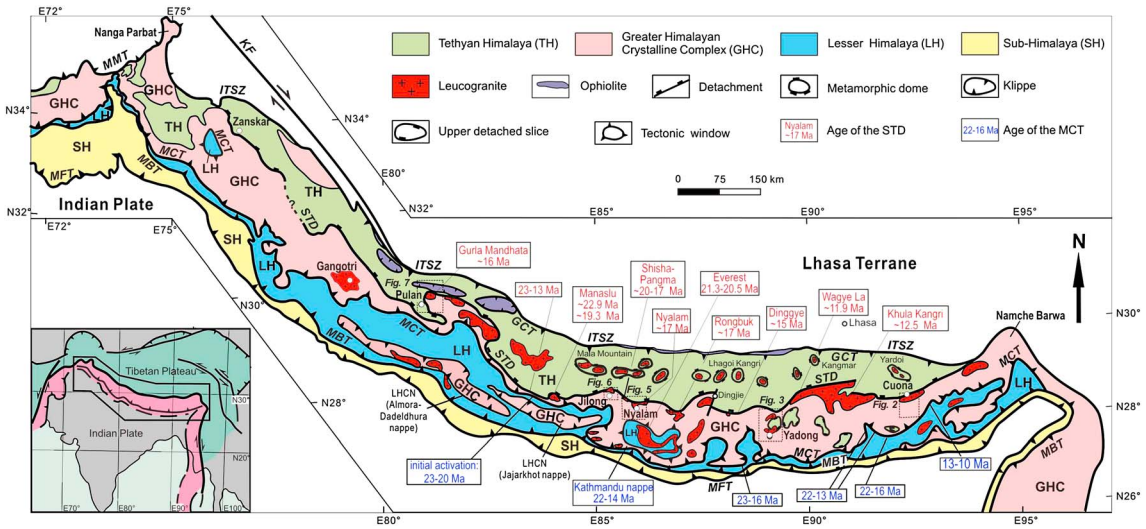

Figure 1. Simplified geologic map of the Himalayan orogen (from *DiPietro and Pogue*, [2004]; *Yin*, [2006]; *Pêcher et al*., [2008]). Abbreviations: GHC, Great Himalayan Crystalline; LH, Lesser Himalaya; SH, Sub-Himalaya; TH, Tethyan Himalaya; LHCN, Lesser Himalayan crystalline nappes; ITSZ, Indus-Tsangbo suture zone; GCT, Great Counter Thrust; KF, Karakoram Fault; MBT, Main Boundary Thrust; MCT, Main Central Thrust; MFT, Main Front Thrust; STD, South Tibet Detachment. Boxes in dashed lines show study areas. Inset shows major boundary faults in the Himalayan orogen and the Tibetan Plateau. A summary of U-Th-Pb ages of monazite and $^{40}Ar/^{39}Ar$ cooling ages of mica is given for leucogranites in the footwall of the STD (in red) and activation time of the MCT (in dark blue). References for the STD: Khula Kangri [*Edwards et al*., 1996; *Edwards and Harrison*, 1997], Wagye La [*Wu et al*., 1998], Dinggye [*Xu*, 1990; *Leloup et al*., 2010], Rongbuk [*Murphy and Harrison*, 1999], Nyalam [*Schärer et al*., 1986; *Xu*, 1990], Everest [*Simpson et al*., 2000], Shisha-Pangma [*Searle et al*., 1997], Manaslu [*Harrison et al*., 1999], Annapurna Range [*Hodges et al*., 1996], and Gurla Mandhata [*Wang et al*., 2005]. References for the MCT from east to west: Arunachal Himalaya [*Yin et al*., 2010b], Bhutan [*Grujic et al*., 2002], Sikkim [*Harris et al*., 2004], Kathmandu nappe [*Metcalfe*, 1993; *Stephenson et al*., 2001], Annapurna Range [*Hodges et al*., 1996].

[3] Meanwhile, orogen-parallel stretching lineation has been observed in a few areas in the upper part of the GHC, including the Nyalam area in southern Tibet [*Brun et al*., 1985], central Nepal [*Pêcher*, 1991; *Pêcher et al*., 1991; *Coleman*, 1996], and Garhwal [*Pêcher and Scaillet*, 1989] and Ladakh areas in the western Himalaya [*Epard and Steck*, 2004]. Orogen-parallel ductile detachments were also recognized at the roofs of transverse domes deforming or cutting across the STD, e.g., in the Gurla Mandhata area in SW Tibet [*Murphy et al*., 2002], the Leo Pargil dome in NW India [*Thiede et al*., 2006; *Langille et al*., 2012], and the Ama Drime massif in Tibet-Nepal [*Jessup et al*., 2008; *Langille et al*., 2010]. The timing, mechanisms, and regional significance of the orogen-parallel ductile deformation for exhumation of the GHC are still under debate. Possible large-scale lateral ductile flow as a consequence of the radial convergence on an arc-shaped boundary has been proposed to explain Miocene extrusion of the middle crust in the Nanga Parbat massif in the western Himalaya [*Seeber and Pêcher*, 1991]. Recently, *Murphy et al*. [2009] proposed that a foreland propagation fault system could accommodate outward radial expansion of the Himalayan orogen and could result in arc-parallel extension in the Zada basin in SW Tibet. However, given heterogeneity in the general radial Himalayan pattern, orogen-parallel stretching structures in the GHC are often regarded as a local feature due to strain partitioning in the STD [*Yin*, 2006]. Most 2D or pseudo-3D models for evolution of the Himalayan orogen are based on north-south sections [e.g., *Burchfiel and Royden*, 1985; *Chemenda et al*., 1995, 2000; *Henry et al*., 1997; *Beaumont et al*., 2001; *Grujic et al*., 2002; *Robinson et al*., 2003].

[4] To evaluate the regional significance of lateral flow in accommodating the growth of the Himalayan orogen, some key questions must to be addressed. What are the spatial distribution and tectonic settings of orogen-parallel stretching structures? When did they develop, and what deformation conditions did they experience? How did they interact or correlate with the STD and MCT bounding the upper and lower surfaces of the GHC? In addition, systematic studies of Pliocene-Quaternary brittle deformation [*Hurtado et al*., 2001; *Pêcher et al*., 2008] as well as GPS geodetic velocities [*Styron et al*., 2011] indicate that orogen-parallel extension is an important component of recent and present-day Himalayan deformation. Did it also play an important role in the exhumation of the GHC in the Miocene? Answers to these questions are not only critical for constructing evolution models of the Himalayan orogen, but also important for our understanding of continental collision zones.

[5] This paper presents an integrated study of field mapping, microstructure analysis, and geochronology in the Cuona, Yadong, Nyalam, Jilong, and Pulan areas, southern Tibet. In all the five areas, we find ductile shear zones in the GHC with gently dipping foliation and a penetrative east-west trending

stretching lineation. Based on electron backscatter diffraction (EBSD) measurements of quartz, zircon U-Pb dating by sensitive high-resolution ion microprobe (SHRIMP) and laser ablation multi-collector inductively coupled plasma mass spectrometry (LA-MC-ICP-MS), and $^{40}Ar/^{39}Ar$ cooling ages of biotite and muscovite, we constrain deformation conditions and timing of the orogen-parallel ductile extension. The results bring new insights into the Himalayan extrusion/extension models.

2. Geological Setting

[6] The Himalayan orogen is bounded by the Indus-Tsangpo suture zone in the north and the Main Frontal Thrust in the south. Along the strike, over more than 2000 km from Zanskar to Namche Barwa, the Himalayan orogen can be divided into four juxtaposed tectono-stratigraphic zones from north to south: the Tethyan Himalaya (TH), the GHC, the Lesser Himalaya (LH), and the Sub-Himalaya (SH), which are separated by the STD, the MCT, and the Main Boundary Thrust (MBT), respectively (Figure 1) [e.g., *Burg et al*., 1984; *Burchfiel et al*., 1992; *Le Fort*, 1996; *Garzanti*, 1999; *Wyss et al*., 1999; *DeCelles et al*., 2001; *DiPietro and Pogue*, 2004; *Yin*, 2006; *Searle et al*., 2008]. The exposed GHC is generally composed of Neoarchean to early Paleozoic amphibolite to granulite facies gneisses, amphibolites, marbles, granulites, and migmatites, which are known as the Nyalam group in southern Tibet [*Zhang and Li*, 1981; *Xu et al*., 2005] and the Namche Barwa group in the eastern Himalayan syntaxis [*Liu and Zhong*, 1997; *Burg et al*., 1998; *Ding et al*., 2001]. In addition, the early to middle Miocene leucogranites widely intrude the GHC, especially near the STD [e.g., *Hodges et al*., 1992; *Searle et al*., 1997; *Guillot et al*., 1999; *Streule et al*., 2010].

[7] The STD is a moderately north-dipping fault system that juxtaposes the Proterozoic to Eocene Tethyan Himalaya Sequence over the GHC [e.g., *Burg et al*., 1984, *Burchfiel et al*., 1992; *Yin*, 2006]. In many sections, the STD is composed of two superimposed detachment faults such as in the Everest area [*Carosi et al*., 1998; *Murphy and Harrison*, 1999; *Searle*, 1999; *Law et al*., 2011], in the Annapurna-Manaslu area [*Searle and Godin*, 2003]. In several areas, the topographic break between the GHC and the Tibetan Plateau follows a brittle normal fault, which crosscuts the mylonites of the STD [e.g., Dzong Chu fault, *Edwards et al*., 1999; *Kellett and Grujic*, 2012]. The peak metamorphic temperature of the structurally lower strands of the STD can reach ~650 °C [e.g., in the Everest area, *Jessup et al*., 2008; *Cottle et al*., 2011]. The hanging wall of the STD shows a right-way-up metamorphic pattern across many kilometers, from ~650–500 °C at the base to unmetamorphosed sedimentary rocks at high structural level [*Herren*, 1987; *Crouzet et al*., 2007; *Chambers et al*., 2009; *Kellett et al*., 2010]. The STD is generally interpreted as a low-angle detachment with top-to-the-north shear sense, either as the roof boundary of the exhumed Himalayan prism or as the upper boundary of the exhumed middle crustal GHC rocks by a channel flow process [*Beaumont et al*., 2001; *Godin et al*., 2006; *Kellett and Grujic*, 2012]. However, both top-to-the-north (normal faulting) and top-to-the-south (thrusting) motions have been recognized in the STD [*Hodges et al*., 1996; *Carosi et al*., 1998, 1999; *Godin et al*., 1999]. Recent studies reveal that the southern extent of the STD merges with the MCT and bounds the leading edge of the GHC in NW India [*Webb et al*., 2007, 2011a] and in central Nepal [*Webb et al*., 2011b], suggesting that the STD could be a back thrust linked with the Great Counter Thrust to the north. This tectonic wedging model can better explain the stratigraphic continuity of the LH, GHC, and TH in northern Pakistan in the western Himalaya [*Pogue et al*., 1999; *DiPietro and Pogue*, 2004] and the depositional contact between the GHC and TH in the central Bhutan Himalaya [*Long and McQuarrie*, 2010].

[8] The precise timing of motion on the STD is mainly based on indirect assumptions (emplacement dating of leucogranites related to exhumation of the GHC), or more precisely bracketed by ages of granitic massifs or dykes that either cut across mylonitic fabrics of the STD (youngest bracket) or crystallized before the solid-state mylonitic fabric (oldest bracket). As shown in Figure 1, activation of the STD is constrained by leucogranites dated mostly at ~23–19 Ma, but some leucogranites are as young as 12 Ma (Wagye La and Khula Kangri granite in eastern Himalaya). These leucogranites were emplaced during active motion on the STD, often in a multiple-step process. For instance, the Manaslu granite in the central Himalaya has two main crystallization periods at ~22.9 and 19.3 Ma [*Harrison et al*., 1999]. The STD in the Annapurna Range in Nepal activated with the MCT at 22.5 Ma, which was followed by an out-of-sequence thrust between 22.5–18.5 Ma and top-to-the-south extension after 18.5 Ma [*Hodges et al*., 1996]. In addition, ductile deformation along the STD in the NW Himalaya may have ceased by the end of the middle Miocene, as indicated by $^{40}Ar/^{39}Ar$ cooling ages of biotite and muscovite from the immediate STD hanging wall and footwall [*Vannay et al*., 2004; *Thiede et al*., 2005; *Cottle et al*., 2011].

[9] Juxtaposing the GHC over the Proterozoic to Cambrian low-grade metamorphic rocks of the Lesser Himalaya, the MCT is a 2 to 10 km-thick ductile shear zone characterized by inverted metamorphism and top-to-the-south shear fabrics [e.g., *Pêcher*, 1989; *Harrison et al*., 1997; *Searle et al*., 2008; *Corrie and Kohn*, 2011]. In the central Himalaya, it is actually possible to recognize two thrust zones of strain concentration in the MCT: an upper MCT (MCT-2) [*Arita*, 1983] at the top of the shear zone, immediately below the high-grade GHC rocks, and a lower MCT (the MCT root zone or MCT-1) within the LH sequence. The MCT in Nepal exhibits a ramp-flat geometry: a steeply north-dipping ramp in the north (MCT-1) is relayed in the south by a flat thrust, folded in broad antiforms and synforms [*DeCelles et al*., 2001]. This pattern is quite similar to the geometry of the MCT in the NW Indian Himalaya [*Yin*, 2006; *Webb et al*., 2007]. Above the thrust flat of the MCT-1, low- to medium-grade metamorphic rocks are exposed as Lesser Himalayan Crystalline Nappes (LHCN), preserved in the synforms. The origin of the LHCN from the GHC or TH is still debated [e.g., *Upreti and Le Fort*, 1999; *Webb et al*., 2011b].

[10] Initial activation of the MCT is still poorly constrained, but exhumation along the MCT has been dated by numerous cooling ages, either in the hanging wall of the MCT-2 where retrograde metamorphism accompanied exhumation of the GHC or in its footwall where the prograde "reverse metamorphism" developed in the MCT shear zone itself (Figure 1). For instance, the MCT-2 in central Nepal was active at 23–20 Ma

based on hornblende $^{40}Ar/^{39}Ar$ and monazite U-Pb ages and may have continued to accommodate episodic shortening as young as the Pliocene [*Hubbard and Harrison*, 1989; *Hodges et al*., 1996; *Coleman*, 1998]. Meanwhile, motion along the MCT-1 occurred between 22 and 14 Ma in the Kathmandu Nappe [*Arita et al*., 1997; *Johnson and Rogers*, 1997; *Johnson et al*., 2001], and the southernmost portion of the MCT-1 ceased motion since 14 Ma [*Arita et al*., 1997]. The MCT was active at 23–16 Ma in Sikkim [*Harris et al*., 2004; *Catlos et al*., 2004]. Similar ages of 22–16 Ma are reported for the MCT in Bhutan, followed by the activation of the out-of-sequence Kakhtang thrust in the MCT hanging wall at 14–10 Ma [*Grujic et al*., 2002]. Farther to the east, the MCT in the eastern Himalaya of NE India forms the roof of a major thrust duplex. Its initiation occurred at ~13 Ma in the northern part and at ~10 Ma in the southern part [*Yin et al*., 2010b]. In brief, cooling ages show nearly coeval activation of the STD and MCT under ductile conditions from at least 23 to 10 Ma, with younger ages in the eastern Himalaya than in the western Himalaya.

3. Field Observations

[11] We investigated five areas in southern Tibet: the Cuona (92°E), Yadong (89°E), Nyalam (86°E), Jilong (85.3°E), and Pulan (Gurla Mandhata, 81.2°E) areas (Figure 1). Based on systematic measurements of the foliation (metamorphic and mylonitic foliations) and stretching lineation, ductile shear zones are recognized in the high-grade GHC rocks in these areas, which are characterized by high strain (mylonites or mylonitic rocks), gently dipping foliation, and nearly east-west trending stretching lineation.

3.1. The Cuona Area in Eastern GHC

[12] Cuona County is located in the eastern Himalaya where the orogen becomes ENE striking (Figure 1). The GHC in this area is composed of strongly deformed granitic gneisses, sillimanite-garnet-biotite gneisses, marbles, and garnet-graphite schists. As shown in Figure 2a, about 10 km south of Cuona County, the nearly east-west striking STD juxtaposes chlorite-biotite-garnet schists and limestones of Cambrian age [*Geological Survey of Yunnan Province*, 2005, unpublished map and report] in its hanging wall over high-grade Proterozoic GHC gneisses in its footwall. To the north of the STD, a north-dipping normal fault separates Upper Triassic sandstones, slates, basalts, and tuffs above and Cambrian sedimentary rocks below. A granitic pluton intruded into the Upper Triassic rocks at 20.1–12.1 Ma according to K-Ar dating, which may be related to the activation of the STD [*Geological Survey of Yunnan Province*, 2005, unpublished report]. The intensive deformation in the GHC is characterized by a gently dipping foliation and two groups of penetrative stretching lineation (Figure 2b). In the north part of the Cuona-Mama section, the stretching lineation of the high-grade GHC rocks trends N-S when close to the STD (Figures 2c and 2d). Farther to the south, the stretching lineation changes to NE and ENE trending near Mama village (Figures 2e and 2f). Synmylonitic asymmetric folds and other shear fabrics near Mama village indicate a top-to-the-NE or top-to-the-ENE shear sense for these rocks.

3.2. The Yadong Area in Eastern GHC

[13] About 250 km west of Cuona County, the Yadong area is characterized by a Paleozoic sedimentary cover resting on high-grade GHC basement at ~10 km south of the STD (Figure 3). The GHC basement is exposed as garnet-sillimanite-amphibole-plagioclase gneisses, amphibolites, marbles, and granitic gneisses. Above the crystalline basement, the Tethyan Himalayan Sequence contains Cambrian garnet-bearing biotite schists, chlorite schists, and calcischists intercalated with meta-sandstones, Ordovician limestones, calcisiltites and phyllites, Silurian sandstones, limestones and shales, and Devonian-Triassic shales intercalated with limestones and marbles. It is noteworthy that the metasedimentary rocks in the south have lower metamorphic grade than those in the hanging wall of the STD.

[14] Close to the STD, the high-grade GHC rocks display a strong shear fabric with a nearly north-south trending stretching lineation and a top-to-the-north shear sense (Figure 3a). Farther south, the contact between the low-grade sedimentary strata and the high-grade GHC basement appears as a low-angle shear zone, which has been gently refolded about a wide syncline (Figure 3b). We refer to it as the Yadong shear zone. North of Dongli village, the stretching lineation on the Yadong shear zone is east-west trending (Figure 3c) and has developed in a penetrative manner both in the footwall (mylonites, mylonitic gneisses, and migmatites) (Figures 4a–4c) and hanging wall (phyllites and recumbent folds of limestones) (Figures 4d and 4e). However, to the south of Dongli village, the lineation turns to NW-SE trending (Figure 3d). As there is no cartographic continuity between the STD and the Yadong shear zone, a link between both is unclear. The Yadong shear zone could be a flat prolongation to the south of the STD: the geometry of the STD being then very similar to what is observed in the Kula Kangri area [*Edwards et al*., 1999] or in the Beas area [*Wyss et al*., 1999]. However, similar with the observation in the Cuonan area (Figure 2b), the stretching lineation in the Yadong area does not show progressive rotation from the Yadong shear zone to the STD (Figures 3c and 3d), rather suggesting that the Yadong shear zone and the STD are two independent structures. $^{40}Ar/^{39}Ar$ cooling ages of biotite and muscovite yield 14.9–13.5 Ma for leucogranite intrusion in the Yadong area [*Liu et al*., 2004]. Because the leucogranites cut mylonitic fabrics of the Yadong shear zone, initiation of the Yadong shear zone should occur prior to 15 Ma.

[15] At outcrop, numerous shear-sense criteria (geometry of feldspar lenses, asymmetric boudinage of felsic veins, asymmetric sub-recumbent folds) indicate a dominant top-to-the-east or top-to-the-SE shearing (Figures 4c and 4d), which is consistent with the microstructures (asymmetric garnet pressure shadow, rotational synkinematic fibrolitic sillimanite, and S/C structures) of mylonitic gneisses in the footwall (Figures 4f–4h) and schists in the hanging wall (Figure 4k). To exclude potential thermal effects of the leucogranite intrusion, we select samples to the south of Dongli village to estimate the deformation temperature of the Yadong shear zone. The peak metamorphic temperature of the Yadong shear zone reached 650–700 °C, according to the growth of prismatic sillimanite and myrmekite (Figure 4i) and chessboard extinction of quartz (Figure 4j) in Sil-Grt-Qtz-Bt gneiss. It is noteworthy that deformation intensity and metamorphic grade decrease upward across the Yadong shear zone, as expressed by changes from high-amphibolite facies gneisses and mylonites in the footwall to greenschists and phyllites in the immediate hanging wall.

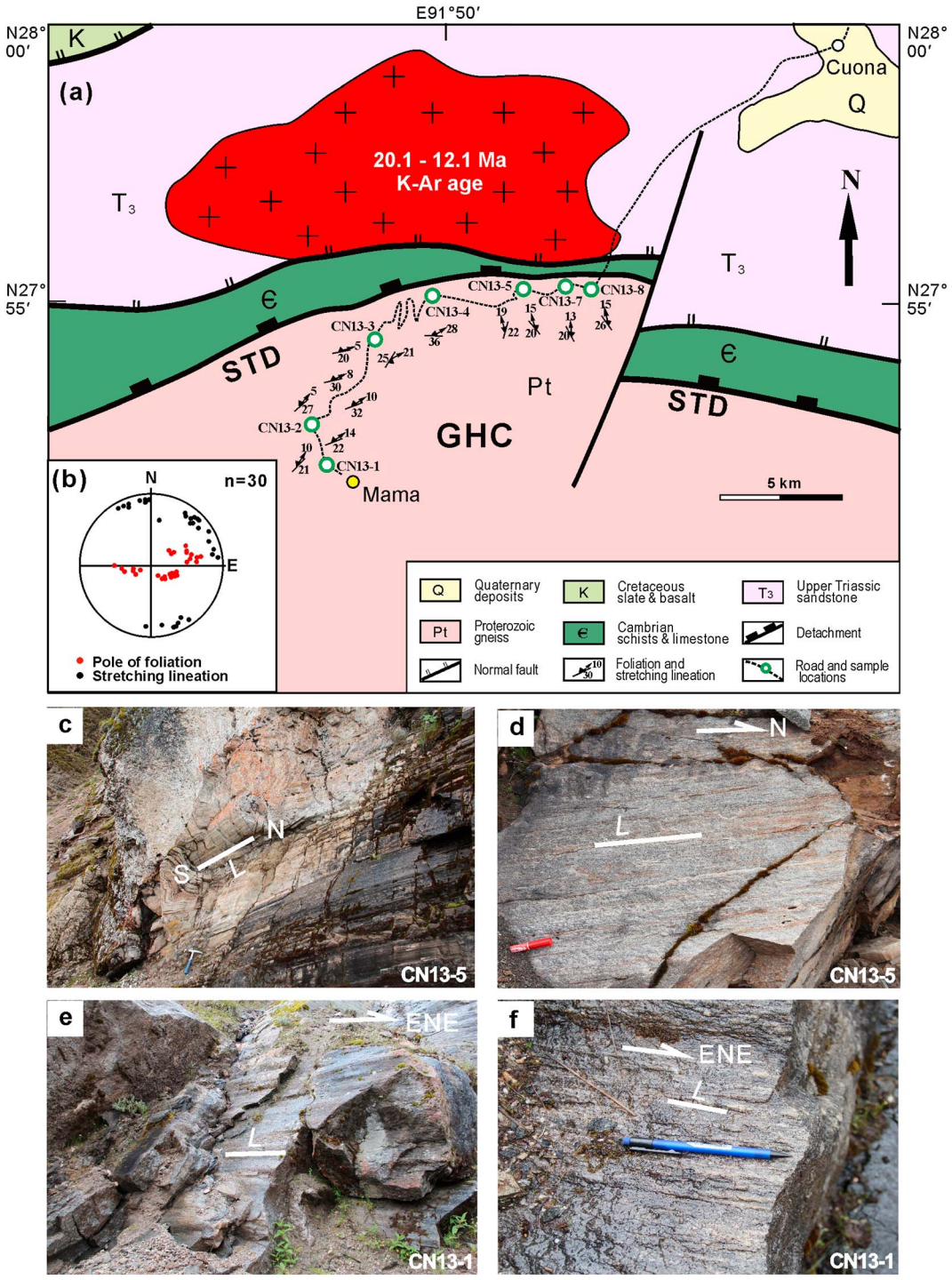

Figure 2. (a) Simplified geologic map of the Cuona area after the 1: 250,000 geological map of the Cuona County (China) (from [*Geological Survey of Yunnan Province*, 2005, unpublished]). (b) Lower hemisphereprojection for stretching lineation and pole of foliation of the GHC mylonites, gneisses, schists, and marbles. (c, d) North trending stretching lineation in the footwall of the STD. (e, f) ENE trending stretching lineation near Mama village.

[16] Taking into account the similar deformation styles of the GHC rocks in the Yadong and Cuona areas, we propose that the Yadong shear zone with its east-west trending stretching lineation and top-to-the-east shear fabrics in the Yadong area extends eastward to the Cuona area, but it rotates to a ENE trending stretching lineation with top-to-the-ENE shear fabrics along the strike of the orogen. The observations in both areas demonstrate significant orogen-parallel ductile stretching in the eastern GHC.

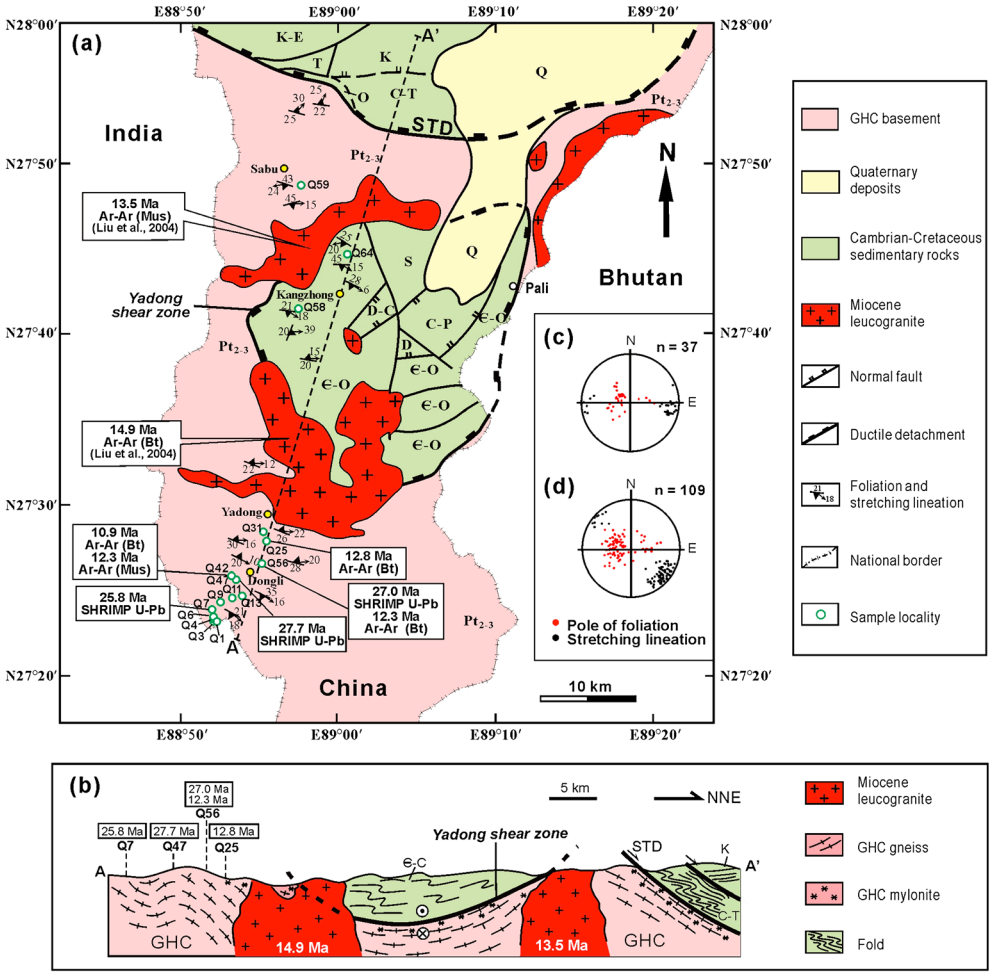

Figure 3. (a) Simplified geologic map of the Yadong area after the 1: 250,000 geological map of the Yadong County (China) (from [*China University of Geosciences*, 2005, unpublished]). (b) A nearly north-south cross section. Lower hemisphere projection for stretching lineation and pole of foliation of the Yadong shear zone (c) to the north of Dongli village and (d) to the south of Dongli village.

3.3. The Nyalam Area in Central GHC

[17] The GHC in the Nyalam area consists of amphibolite facies gneisses, marbles, and migmatites. In the northern part of the Nyalam area, the nearly east-west striking STD places Tethyan Cambrian-Ordovician limestones, slates, and phyllites over the GHC (Figure 5a). *Brun et al.* [1985] first evidenced in the Nyalam area several slices in the GHC bounded by high-temperature mylonitic zones. A broad antiform smoothly refolds the gneiss pile. The stretching lineation progressively rotates from N10–20°E to N90–100°E in the two lower slices, and it trends predominantly N90°E in the two upper slices. They assessed a bulk orogen-parallel top-to-the-west shearing in this region. *Burchfiel et al.* [1992] reported that ~30 km to the north of Nyalam, an approximated N-S stretching lineation developed in the immediate hanging wall and footwall of the STD.

[18] This study confirms the previous observations along the Nyalam-Zham section through systematic field mapping and microstructural analysis using the EBSD technique (in next section). Stretching lineation in the GHC trends quite regularly to N110°E (Figure 5b) and is particularly well defined by the orientation of sillimanite and boudinage of felsic veins (Figures 5c and 5d). However, the shear sense in the high-grade GHC rocks is irregular. Both top-to-the-west and, more often, top-to-the-east shear fabrics are indicated by non-coaxial deformation criteria, such as asymmetric pressure shadows, rotated garnets, drag folds, σ-shaped porphyroclasts, and S/C texture (Figures 5d–5f). In contrast to the Yadong shear zone in the eastern GHC, it is likely that the sedimentary cover in the hanging wall and the uppermost part of the footwall (high-grade mylonitic GHC rocks) have been eroded away. Therefore, we refer to the Nyalam shear zone as a relic ductile shear zone with east-west trending lineation between the GHC basement and its sedimentary cover.

3.4. The Jilong Area in Central GHC

[19] The Jilong area is located ~60 km west of the Nyalam area (Figure 1). The GHC in the Jilong area is similar to that in the Nyalam area, but it was intruded by leucogranites near the STD (Figure 6). $^{40}Ar/^{39}Ar$ dating of muscovite and biotite in mylonites within the STD and from its footwall recorded rapid exhumation of the GHC in the middle Miocene (16–15 Ma) [*Wang et al.*, 2006]. South of the STD, mylonitic gneisses in the lower part of a gneissic dome

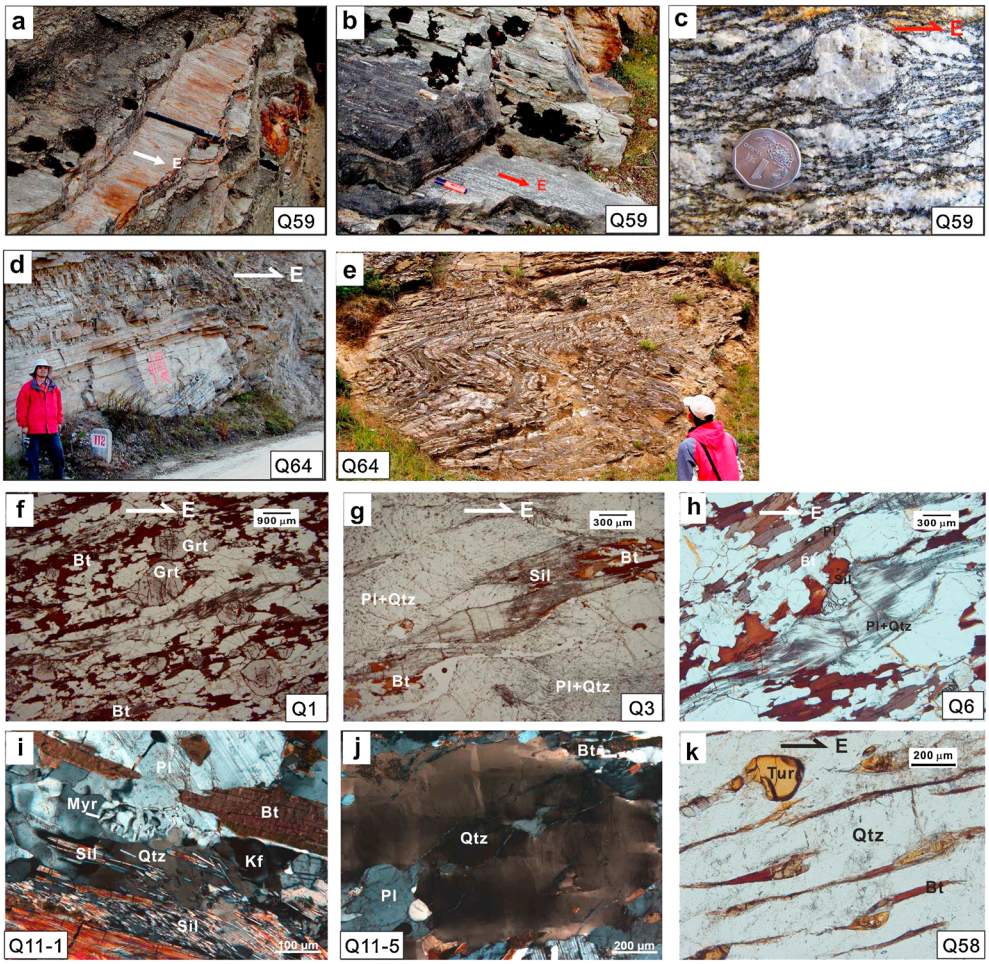

Figure 4. Outcrop observations and microphotographs of the Yadong shear zone, showing a top-to-the-east shearing in both the hanging wall and footwall rocks. (a) East-west trending stretching lineation in schist and (b) felsic gneiss in the footwall near Sabu village. (c) σ-Type felsic vein in the GHC augen gneiss in the footwall near Sabu village. (d) Recumbent fold in the Ordovician limestone in the hanging wall. (e) Recumbent fold in the Silurian sandstone and shale characterized by the stretching lineation parallel to the fold axis. (f) Asymmetric pressure shadow of garnet in mylonitic Grt-Bt-Pl gneiss. (g, h) S/C fabric defined by synkinematic fibrolitic sillimanite in Grt-Sil-Bt-Pl mylonite. (i) Prismatic sillimanite and myrmekite texture. (j) Chessboard extinction of quartz in Sil-Grt-Qtz-Bt gneiss in the footwall near Dongli village. (k) σ-Type porphyroclasts of tourmaline and altered plagioclase with tails of biotite in the hanging wall mylonitic Qtz-Bt schist. Abbreviations: Bt, biotite; Grt, garnet; Kf, K-feldspar; Pl, plagioclase; Qtz, quartz; Myr, myrmekite; Sil, sillimanite; Tur, turmaline. Sections are parallel to the lineation and normal to the foliation.

are characterized by a strong east-west stretching lineation and both top-to-the-east and top-to-the-west shear senses. Farther south, the lineation turns to SSE trending in the lower part of the GHC, which may be related to southward thrusting along the MCT. In thin sections of felsic mylonites H44-4 and H44-5, core-and-mantel structures of plagioclase and strongly elongated quartz ribbons suggest deformation at high temperature and high strain rate (Figures 6b and 6c). The Nyalam shear zone probably extends westward into the Jilong area.

3.5. The Pulan Area in Western GHC

[20] Our westernmost study area is the Pulan area on the western flank of the Gurla Mandhata dome. Previous investigations have identified four main lithotectonic units in this area: the Yungbwa ophiolite (also known as the Pulan ophiolitic nappe), the Tethyan fold-and-thrust belt, the Gurla Mandhata metamorphic dome, and the north-south trending Pulan basin with Tertiary-Quaternary sediments (Figure 7) [*Cheng and Xu*, 1987, *Murphy et al*., 2002; *Geological Survey of Hebei Province*, 2005, unpublished map and report].

[21] *Murphy et al*. [2002] proposed that the western contact of the Gurla Mandhata dome with the Pulan basin follows a pair of west-dipping low-angle (<45°) normal faults: the older Gurla Mandhata detachment fault 1 ($GMDF_1$) places weakly metamorphosed lower Paleozoic phyllites and marbles over a thick (>2 km) section of amphibolite facies mylonitic schists, gneisses, marbles, and variably deformed leucogranites, while the younger and structurally higher brittle Gurla Mandhata detachment fault 2 ($GMDF_2$) places Tertiary

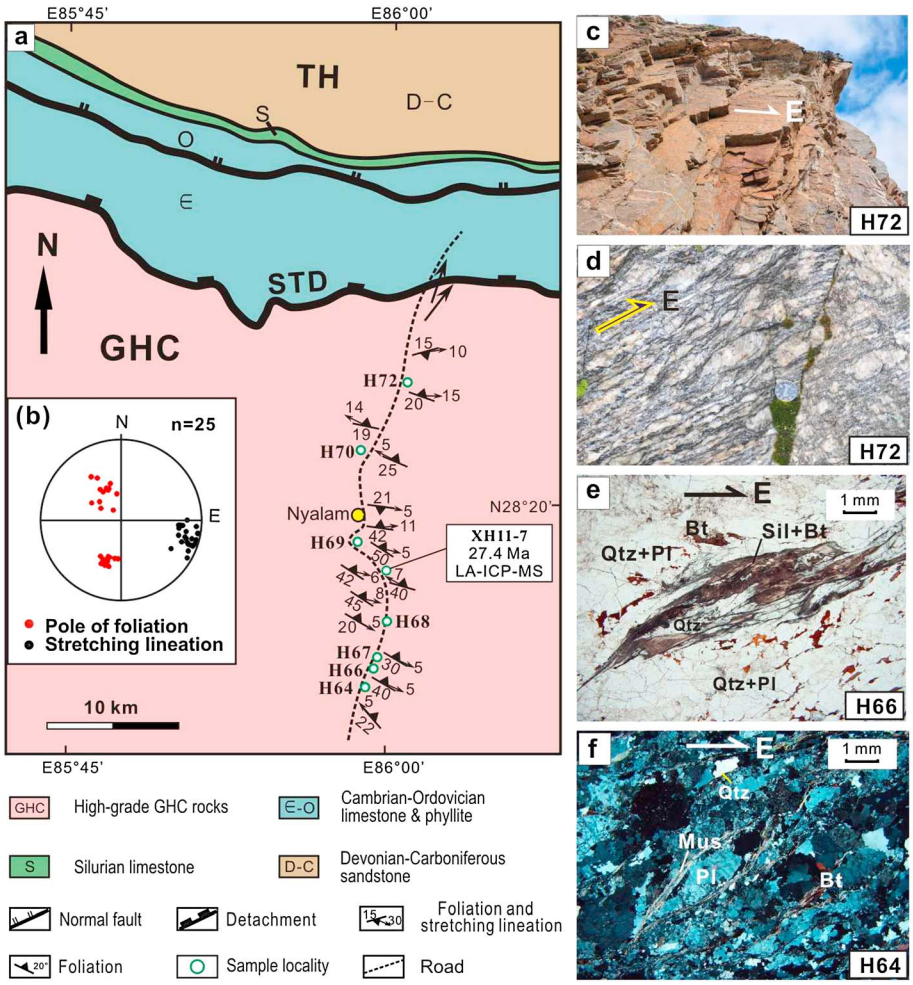

Figure 5. (a) Simplified geologic map of the Nyalam area after the 1: 250,000 geological map of the Nyalam County (China) (from [*Chengdu Institute of Geology and Mineral Resources*, 2002, unpublished]). (b) Lower hemisphere projection for stretching lineation and pole of foliation near Nyalam village. East-west trending stretching (c) in marbles and (d) in augen gneiss. (e) Stretching sillimanite in mylonitic Sil-Bt-Pl gneiss. (f) σ-Type plagioclase porphyroclasts in mylonitic Mus-Bt-Pl gneiss. Sections are parallel to the lineation and normal to the foliation.

sedimentary strata in the hanging wall against the Ordovician phyllites and marbles in its footwall and cuts across the $GMDF_1$. Both Gurla Mandhata detachments exhibit a top-to-the-west shear sense in the western flank of the Gurla Mandhata dome. To the southwest in Nepal, the $GMDF_1$ and $GMDF_2$ merge in the WNW striking, normal right-slip Gurla Mandhata-Humla fault system, which splits still farther east into two branches: the northern branch cuts across the GHC in western Nepal and might transfer a part of movement of the Karakorum fault onto the MCT, while the southern branch seems to cut the STD to the south of the Saipal summit in Nepal [*Murphy and Copeland*, 2005].

[22] This study adds new structural and geochronological data about the Gurla Mandhata dome. Various high-amphibolite facies rocks (augen gneisses, garnet-amphibole-plagioclase gneisses, sillimanite-garnet-biotite-plagioclase gneisses, garnet amphibolites, marbles, and migmatites), which were intruded by leucogranites at 16 Ma [*Wang et al.*, 2005], form the core of the Gurla Mandhata dome. Consistent with field observations in the footwall rocks of the $GMDF_1$ by *Murphy et al.* [2002], these rocks consist of a mylonitic shear zone with a foliation dipping gently to NNE or SSW because of the dome structure. A remarkable nearly east-west trending sub-horizontal lineation (Figure 7c) is defined by the alignment of sillimanite and hornblende, recumbent folds, and boudinage of felsic veins (Figures 8a and 8b). A top-to-the-west shear sense can be clearly determined according to asymmetric folds of mylonitic marbles and S/C texture in felsic gneisses at outcrop (Figures 8a and 8b) as well as σ- and δ-type porphyroclasts of plagioclase, recumbent folds, and domino structures in thin sections (Figures 8c–8g). This extensional ductile shear zone was formed under high-grade metamorphic conditions, probably up to 700 °C, as evidenced by undulose extinction, core-and-mantle structures, and subgrain structures of feldspar porphyroclasts (Figures 8e–8g), strongly elongated strain-free quartz ribbons (Figure 8g), and growth of myrmekite during shearing (Figure 8h).

[23] Combining the previous studies with our new field observations and geochronological data (see section 5), we present an alternative structural framework for the Gurla Mandhata dome (Figure 7). The brittle $GMDF_2$ overprints

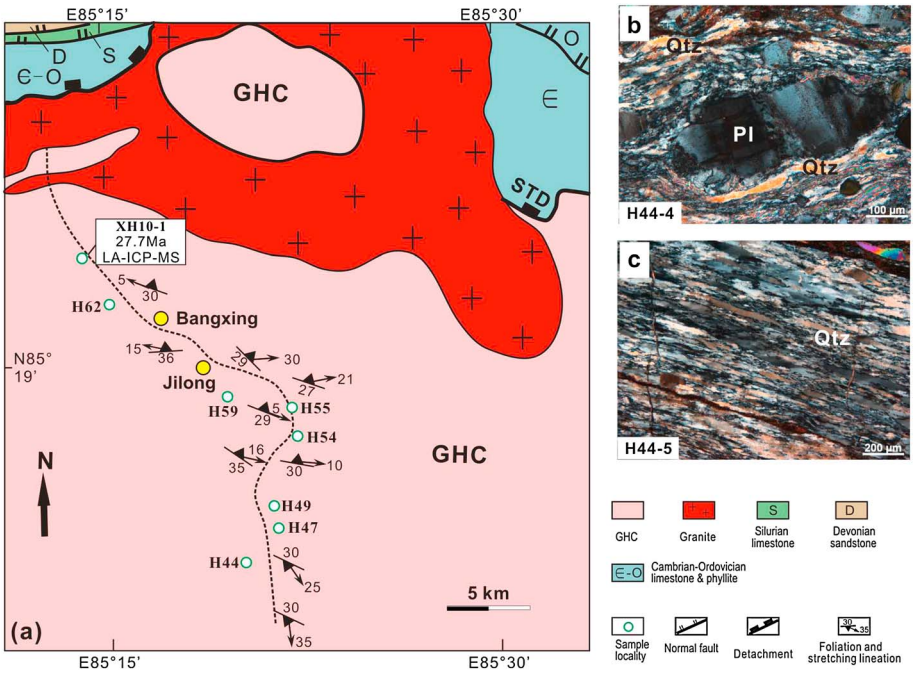

Figure 6. (a) Simplified geologic map of the Jilong area after the 1: 250,000 geological map of the Jilong County (China) (from [*Geological Survey of Hebei Province*, 2002, unpublished]), showing east-west trending stretching lineation near Jilong village and SSE trending lineation to the south. (b) A mantle of plagioclase porphyroclast with undulose extinction surrounded by quartz ribbons in felsic mylonite. Notice undulose extinction of plagioclase porphyroclast and the strongly elongated single crystals of quartz in the ribbons. (c) Strongly elongated quartz ribbons in felsic mylonite, probably developed predominantly by subgrain rotation recrystallization. Sections are parallel to the lineation and normal to the foliation.

the ductile contact between the highly metamorphosed basement and the slightly metamorphosed Paleozoic series, which is comparable with the STD elsewhere in the Himalaya. To avoid confusion, we term the older and structurally lower detachment $GMDF_1$ with top-to-the-west ductile normal shearing [*Murphy et al*., 2002] as the Pulan shear zone. Hypothetically, emplacement and shearing of leucogranite dikes in the late Miocene (8.7–6.8 Ma) in the western margin of the Gurla Mandahata dome could be related to the activation of the STD, instead of the $GMDF_1$ as proposed by *Murphy et al*. (2002). In addition, based on the whole-rock Sr and Nd isotopic signatures, *Murphy* [2007] speculated that the Gurla Mandhata metamorphic core is composed of high-grade GHC rocks and the highly metamorphosed and partially melted portion of the Lesser Himalayan metasedimentary rocks. If the isotopic boundary corresponds to the MCT that is composed of amphibolite facies mylonitic gneisses and intruded by leucogranite dikes and sills, as assumed by *Murphy* [2007], the strike of both the STD and MCT would rotate around the Gurla Mandhata dome from east-west in the north, to north-south next to the Pulan basin, and then to WNW in Nepal. However, more work is needed to confirm this hypothesis because isotropic boundaries in the Himalaya commonly, but not always, match tectonic boundaries [e.g., *Yin*, 2006; *Webb et al*., 2011b].

4. EBSD Measurements

[24] Quartz will develop characteristic crystallographic preferred orientation (CPO) under different *P-T* conditions and water fugacity: at 300–400 °C and higher strain rates, a basal slip (0001) < a > is most commonly observed; while at 400–650 °C and lower strain rates, prism slip {m} < a > and rhombohedral slips {r} < a > and {z} < a > become dominant [*Grujic et al*., 1996; *Stipp et al*., 2002; *Passchier and Trouw*, 2005]. The dominant grain boundary migration recrystallization will result in the activation of only the prism slip {m} < a > at 500 °C, while combined basal < a > and prism [c] slips will occur above 630 ± 30 °C, characterized by chessboard extinction with subgrain boundaries parallel to prism and basal planes [*Stipp et al*., 2002]. Above 650 °C, prism slip {m}[c] is active in high-grade metamorphic rocks and subsolidus deformed granites under moderate hydrostatic pressure (350–400 Ma) and geological strain rate [*Blumenfeld et al*., 1986; *Mainprice et al*., 1986]. The late static recrystallization may increase the grain size of quartz and change microstructures. Fortunately, quartz CPO patterns show very minor modification even after strong annealing [*Otani and Wallis*, 2006], which allows us to use quartz fabrics to study the deformation history of a shear zone and infer the distribution of syntectonic paleoisotherms [e.g., *Grujic et al*., 1996; *Law et al*., 2011]. We analyzed the CPOs of quartz using the EBSD technique on a scanning electron microscope JEOL JSM-5610LV in the State Key Laboratory of Continental Tectonics and Dynamics, Institute of Geology, Chinese Academy of Geological Sciences, Beijing. Thin sections for the EBSD analysis were cut parallel to the structural XZ plane (with X parallel to the lineation, Y parallel to foliation and normal to lineation, and

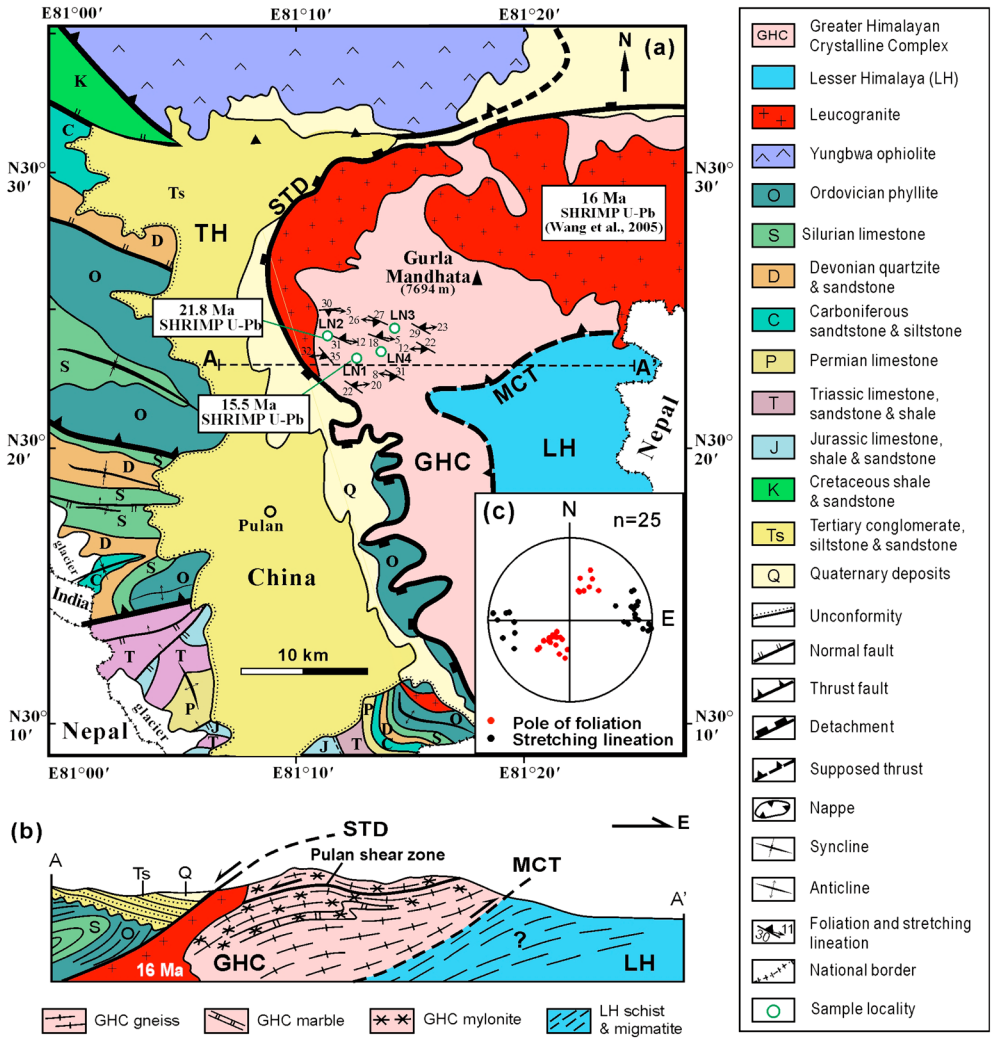

Figure 7. The Pulan area: (a) geologic map and (b) east-west cross section. It is simplified after the 1: 250,000 geological map of the Pulan County (China) (from [*Geological Survey of Hebei Province*, 2005, unpublished]). We interpret the older, ductile Gurla Mandhata detachment fault 1, and the younger, brittle Gurla Mandhata detachment fault 2, shown by *Murphy et al.* [2002] as the Pulan shear zone and the STD, respectively. The isotopic boundary between the GHC and the highly metamorphosed and partial melted LH given by *Murphy* [2007] could be the MCT in this region. (c) Lower hemisphere projection for stretching lineation and pole of foliation of the Pulan shear zone.

Z normal to foliation). Analytical details were given in *Xu et al.* [2009].

[25] For the Yadong shear zone in the eastern GHC, we selected eight mylonitic gneiss samples along the Yadong-Dongli section (Figure 9a). The volume fraction of quartz in samples reaches 20–50%. Abundant recovery and recrystallization structures are observed in thin sections, such as irregular boundaries of recrystallized quartz due to grain boundary migration, quartz ribbons parallel to the lineation, and chessboard extinction of quartz grains. The pole figures of quartz *c*-axis suggest the activation of the asymmetric {m}[c] slip system in samples Q3, Q4, Q6, Q13, and Q31, which is characterized by the maximum concentration of *c*-axes near the lineation with a top-to-the-east shear sense. The predominance of prism [c] slip in these samples suggests a deformation at $T > 650\,^{\circ}C$ [*Mainprice et al.*, 1986], which is consistent with microstructure of quartz and occurrence of sillimanite in the samples. However, samples Q9 and Q12 display the asymmetric basal slip (0001) < a > with the maximum concentration of *c*-axes normal to the foliation and a top-to-the-east shear sense, which is active at low temperature (300–400 °C) and high strain rate. Sample Q11 probably deformed at $T = 400$–$500\,^{\circ}C$, according to the coexistence of prism {m} < a > and basal < a > slips of the quartz.

[26] For the Nyalam shear zone in the central GHC, mylonitic gneisses from the Nyalam and Jilong areas show complex quartz fabrics. In Figure 9b, the predominant prism slip {m} < a > overprints the prism slip {m}[c] and defines a top-to-the-west shear sense in sample H67. In contrast, sample H68 shows both prism [c] and basal < a > slips with a top-to-the-east shear sense, suggesting a dominant grain boundary migration recrystallization at $T > 630 \pm 30^{\circ}$ [*Stipp et al.*, 2002]. With a top-

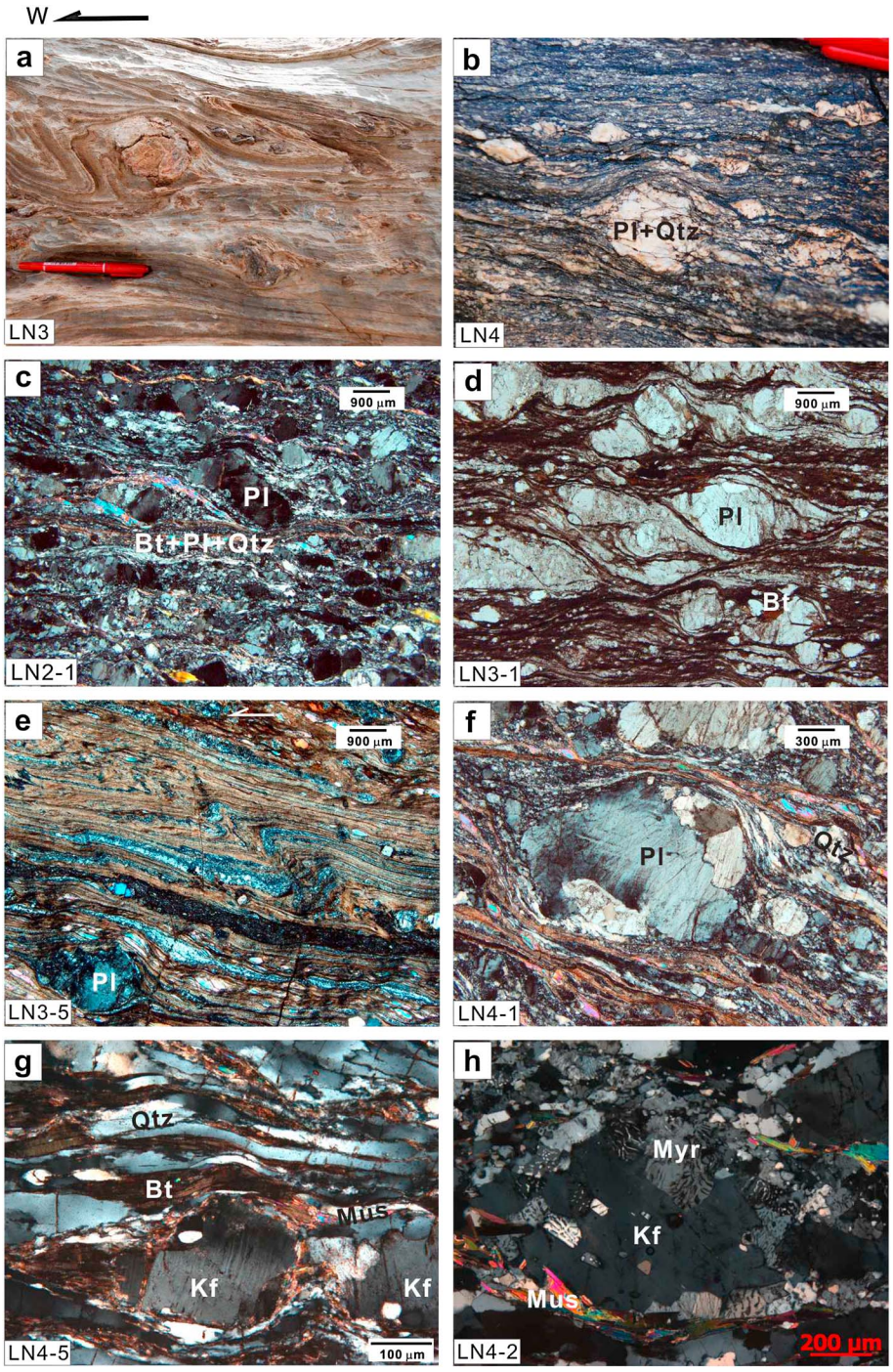

Figure 8. Outcrop observations and microphotographs of the Pulan shear zone, showing a top-to-the-west shear sense. (a) Asymmetric recumbent folds in mylonitic marble. (b) σ-Type felsic veins in mylonitic augen gneiss. (c, d) σ-Type plagioclase porphyroclasts and S/C fabric in mylonitic Bt-Pl gneisses. (e) Asymmetric folding of interlayered fine-grained plagioclase-rich and quartz-rich layers in Qtz-Pl-Bt mylonite. Notice a σ-type mantled porphyroclast of plagioclase (left corner). (f) A plagioclase porphyroclast with undulose extinction and subgrain structures surrounded by dynamic recrystallized quartz and plagioclase in mylonitic Qtz-Pl-Bt gneiss. (g) Strongly elongated quartz ribbons and a K-feldspar porphyroclast with flame-shaped albite lamellae in felsic gneiss. The irregular grain boundaries of feldspar porphyroclasts in Figures 8f and 8g formed by high-temperature grain boundary migration crystallization. (h) Myrmekite "colonies" replacing a K-feldspar porphyroclast around its edge in felsic gneiss. Abbreviations: Bt, biotite; Pl, plagioclase; Kf, K-feldspar; Mus, muscovite; Myr, myrmekite; Qtz, quartz. Sections are parallel to the lineation and normal to the foliation.

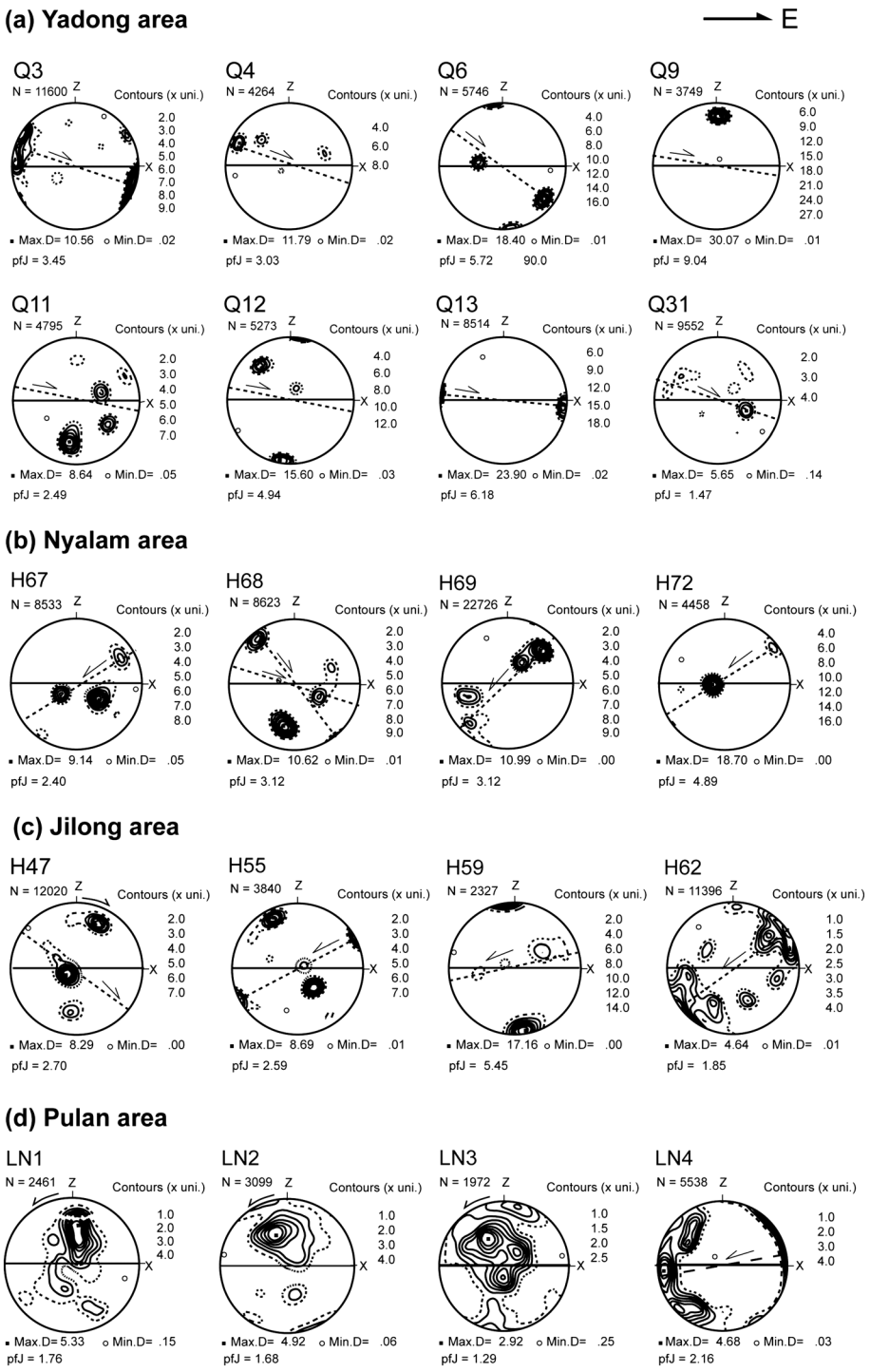

Figure 9. EBSD-measured CPO of quartz in gneisses from (a) the Yadong area, (b) the Nyalam area, (c) the Jilong area, and (d) the Pulan area, southern Tibet. Lower hemisphere equals the area projection. The contours at multiples of a uniform distribution are plotted. Structural directions: X, parallel to the lineation; Z, normal to the foliation. *N*, number of data points; pfJ, texture index. The thick arrow on the upper left corner indicates the trending of the lineation, while dashed line and thin arrow on pole figures presumably represent the inferred slip plane and shear sense, respectively.

to-the-west shear sense, samples H69 and H72 develop predominant prism [c] and prism < a > slips, respectively. For mylonitic gneisses from the southern Jilong area (Figure 9c), samples H47 and H55 show activation of both prism [c] and basal < a > slips. However, shear sense is top-to-the-east for H47 but top-to-the-west for H55. During top-to-the-west shearing, samples H59 and H62 developed basal < a > and prism [c] slips, respectively. Therefore, consistent with field observations, the asymmetric quartz fabrics in the Nyalam shear zone indicate

both top-to-the-west and top-to-the-east shear senses. The quartz CPO patterns suggest a change of deformation temperature from >650 °C to 300–400 °C.

[27] We selected four mylonites and mylonitic gneisses from the Pulan shear zone in the western GHC (Figure 9d). The EBSD measurements reveal a rhombohedral slip {r} < a > in samples LN1 and LN2 and a prism slip {m} < a > in sample LN3, suggesting top-to-the-west shearing under medium-high temperature. Sample LN4 exhibits prism [c] slip with a top-to-the-west shear sense, reflecting a deformation temperature >650 °C.

[28] Compared with the microstructure of samples, EBSD-derived quartz CPO provides consistent information on shear senses and deformation temperature. Different quartz CPO patterns cover a temperature range from 300–400 °C up to 700 °C. However, we do not observe a temperature gradient across the shear zones according to sample locations. Coexistence of predominant high-temperature prism [c] slip and low-temperature basal < a > slip from different samples in one shear zone may have resulted from rapid exhumation from the upper amphibolite to greenschist facies conditions during motion on the shear zones.

5. Geochronological Constraints

[29] In order to bracket "absolute ages" for the dynamothermal events that accompanied orogen-parallel ductile deformation in the GHC, we carried out in situ zircon U-Pb dating using SHRIMP, LA-MC-ICP-MS, and Ar-Ar dating of biotite and muscovite on mylonites and gneisses from the Yadong, Nyalam, and Pulan shear zones.

5.1. U-Pb Dating of Zircon by SHRIMP

[30] We selected three mylonitic Grt-Sil-Pl gneisses (Q7, Q47, and Q56) from the footwall of the Yadong shear zone in the eastern GHC (Figure 3) and two felsic mylonites (LN1 and LN2) from the Pulan shear zone in the western GHC (Figure 7). Zircons were separated using standard heavy liquid and magnetic techniques. Grains were hand-picked and selected on the basis of optical clarity and lack of internal fractures. Zircon grains were mounted in an epoxy disk together with two standards: a primary reference standard zircon M257 with an age of 561 Ma and U content of ~840 μg g^{-1} [*Nasdala et al*., 2008] for U concentration determination, and a secondary reference zircon Temora with an age of 417 Ma [*Black et al*., 2003] for U-Pb age calibration. Analyses were performed on the SHRIMP II ion microprobe in the Beijing SHRIMP Centre, Chinese Academy of Geological Sciences, using the methods of *Williams* [1998]. Each analysis consisted of five scans through the mass range, using a spot size of ~20 μm. The common Pb contribution was corrected using the measured ^{204}Pb and modal common Pb composition [*Stacey and Kramers*, 1975]. The ages were calculated using the decay constant of *Steiger and Jäger* [1977]. Data processing was carried out using the SQUID Excel Marco software by *Ludwig* [2001]. The SHRIMP U-Pb data on zircon for individual analyses are given in Table 1 with uncertainties of 1σ, whereas the uncertainties on weighted mean ages in Figure 11 and the text are given at the 2σ level.

[31] Cathodoluminescence (CL) images of zircon were obtained using a HITACHI S2250-N scanning electron microscope. Samples Q7, Q47, and Q56 contain light brown, round-to-short prismatic, partly irregular zircons, which show a core-rim structure in CL images (Figures 10a–10l). Zircon rims and structureless zircon grains have Th/U < 0.1 (Table 1), suggesting their metamorphic origin. The U-Pb dating of zircon rims and structureless zircon grains yields concordant apparent ages of 23.6–30.1 Ma with a weighted mean ^{206}Pb/^{238}U age of 25.8 ± 0.7 Ma (MSWD = 1.7, for nine analyses) for sample Q7, concordant apparent ages of 25–29 Ma with a weighted mean ^{206}Pb/^{238}U age of 27.7 ± 0.7 Ma (MSWD = 3.8, for nine analyses) for sample Q47, and concordant apparent ages of 23.2–33.0 Ma with a weighted mean ^{206}Pb/^{238}U age of 27.0 ± 0.4 Ma (MSWD = 1.05, for 11 analyses) for sample Q56 (Figures 11a–11c). In contrast, the cores of eight zircons show straight boundaries and strong oscillatory zoning with Th/U of 0.16–0.33, suggesting that they are of magmatic origin (Figure 10 and Table 1). These zircon cores record multiple thermal events in the Paleoproterozoic and the early Paleozoic, with a dominant age population between 560–457 Ma.

[32] CL images of representative zircon grains for two mylonitic felsic gneisses LN1 and LN2 from the Pulan shear zone also reveal a core-rim structure (Figures 10m–10t). As illustrated in Figures 11d and 11e and Table 1, 11 analytical spots on the metamorphic zircon rims of sample LN1 yield concordant ^{206}Pb/^{238}U ages ranging from 14.6 to 16.6 Ma with a weighted mean ^{206}Pb/^{238}U age of 15.5 ± 0.4 Ma (MSWD = 1.12). Notably, both the core and rim of a zircon grain LN1-3-2 (Figure 10n) gave an apparent ^{206}Pb/^{238}U age of 14.6 Ma. Nine analytical spots on the metamorphic zircon rims for sample LN2 produce a weighted mean ^{206}Pb/^{238}U age of 21.8 ± 0.6 Ma (MSWD = 0.54). The cores of zircon in sample LN2 show apparent ^{206}Pb/^{238}U ages of 952, 757, 380, and 323.9 Ma, with Th/U ratios from 0.1 to 0.88 (Table 1). Compared with previous studies in SHRIMP U-Pb dating of zircon from the GHC gneisses [*Xu et al*., 2005; *Zhang et al*., 2008], the ^{206}Pb/^{238}U age of 952 Ma probably reflects the early crystallization of sample LN2, while the relatively young ages of zircon cores are mixture ages.

5.2. U-Pb Dating of Zircon by LA-MC-ICP-MS

[33] LA-MC-ICP-MS can be used to date zircon at high spatial resolution. To constrain the deformation history of the Nyalam shear zone in the central GHC, we collected mylonitic Grt-Sil-Pl gneisses XH11-7 from the Nyalam area (Figure 5) and XH10-1 from the Jilong area (Figure 6). Zircon U-Pb ages were obtained using a ThermoFinnigan Neptune MC-ICP-MS instrument coupled with a New Wave Research UP 213 laser system at the Institute of Mineral Resources, Chinese Academy of Geological Sciences, Beijing. The laser ablation pit size is 25 μm in diameter. Helium was applied as carrier gas, while argon was used as the make-up gas and mixed with the carrier gas. Each analysis incorporated a background acquisition of 20–30 s. Time-drift correction and quantitative calibration for U-Pb dating was performed by ICPMSDataCal [*Liu et al*., 2010]. Zircon GJ1 was used as external standard [*Jackson et al*., 2004]. The concentration of Th and Pb was calibrated according to zircon M127 (with concentration of U = 923 ppm, Th = 439 ppm, Th/U = 0.475, [*Nasdala et al*., 2008]). The Plesovice zircon was dated as an unknown sample and yielded a weighted mean ^{206}Pb/^{238}U age of 337 Ma as reported by *Sláma et al*. [2008]. Instrument details and

Table 1. SHRIMP U-Pb Data on Zircon From Gneisses in the Yadong and Pulan Shear Zones

Analysis Spot	^{206}Pb (%)	^{204}Pb/^{206}Pb	±1σ (%)	U (ppm)	Th (ppm)	^{232}Th/^{238}U	^{206}Pb[a] (ppm)	^{207}Pb/^{206}Pb	±1σ (%)	^{207}Pb/^{235}U	±1σ (%)	^{206}Pb/^{238}U	±1σ (%)	Corr.	Age (Ma)	±1σ (Ma)
Q7																
Q7-1.1	2.15	0.00127	24.861	479	18	0.04	1.62	0.0524	6.16	0.0281	7.16	0.0039	3.64	0.51	25.0	0.9
Q7-1.2	0.06	0.00003	12.890	313	100	0.330	0.055	0.1593	0.44	8.0929	2.38	0.3685	2.34	0.98	2434.2	7.6
Q7-2.1	1.76	0.00104	28.311	876	33	0.04	2.92	0.0453	7.31	0.0239	7.71	0.0038	2.45	0.32	24.7	0.6
Q7-2.2	0.05	0.00003	98.972	502	77	0.159	0.049	0.0638	1.22	0.7971	2.59	0.0906	2.29	0.88	558.9	12.8
Q7-3.1	<0.1	-	50.019	529	23	0.05	1.83	0.0444	15.16	0.0243	15.39	0.0040	2.65	0.17	25.5	0.7
Q7-4.1	10.55	0.00622	25.559	465	24	0.05	1.78	0.0445	24.08	0.0249	24.22	0.0041	2.66	0.11	26.1	0.9
Q7-5.1	0.41	0.00024	44.685	1670	58	0.04	5.66	0.0512	2.99	0.0278	3.81	0.0039	2.35	0.62	25.3	0.6
Q7-6.1	1.99	0.00118	35.080	1139	21	0.02	3.901	0.0478	5.47	0.0261	5.98	0.0040	2.41	0.40	25.4	0.6
Q7-7.1	1.14	0.00067	55.131	727	11	0.02	2.679	0.0411	10.02	0.0240	10.32	0.0042	2.48	0.24	27.2	0.7
Q7-8.1	<0.1	-	61.245	1294	22	0.02	4.715	0.0475	5.12	0.0277	5.74	0.0042	2.58	0.45	27.2	0.7
Q7-8.2	0.08	0.00005	55.665	325	99	0.314	0.081	0.1160	0.56	4.6746	2.35	0.2923	2.28	0.97	1867.2	11.8
Q7-9.1	0.60	0.00036	52.217	2067	46	0.02	7.277	0.0487	4.12	0.0274	4.75	0.0041	2.36	0.50	26.3	0.6
Q47																
Q47-1.1	0.39	0.00021	52.268	4373	43	0.010	16.195	0.0451	4.09	0.0267	4.16	0.0043	0.76	0.18	27.6	0.2
Q47-2.1	0.58	0.00034	30.159	3248	34	0.011	11.448	0.0456	4.11	0.0257	4.72	0.0041	2.32	0.49	26.2	0.6
Q47-2.2	0.05	0.00003	35.356	2195	539	0.245	176.503	0.0579	0.59	0.6849	0.66	0.0858	0.29	0.44	530.8	1.5
Q47-3.1	0.19	0.00011	44.518	5187	57	0.011	20.007	0.0470	2.28	0.0290	3.22	0.0045	2.27	0.71	28.8	0.7
Q47-3.2	0.04	0.00002	28.525	4624	81	0.018	345.887	0.0562	0.45	0.6188	0.63	0.0799	0.43	0.69	495.3	2.1
Q47-4.1	0.43	0.00018	85.691	2647	35	0.014	9.278	0.0472	8.27	0.0264	8.60	0.0041	2.36	0.27	26.1	0.6
Q47-4.2	0.02	0.00001	28.868	9023	167	0.018	748.877	0.0565	0.30	0.6898	0.38	0.0886	0.23	0.60	547.4	1.2
Q47-5.1	0.35	0.00022	64.262	4034	40	0.010	14.907	0.0452	4.08	0.0267	4.71	0.0043	2.35	0.50	27.6	0.6
Q47-6.1	0.42	0.00025	30.941	6441	74	0.012	24.884	0.0457	2.91	0.0282	3.69	0.0045	2.27	0.61	28.8	0.7
Q47-7.1	0.50	0.00029	56.192	3302	32	0.010	12.147	0.0475	5.72	0.0279	6.17	0.0043	2.30	0.37	27.4	0.6
Q47-8.1	0.32	0.00019	30.396	3551	36	0.011	13.296	0.0446	3.65	0.0267	4.30	0.0043	2.28	0.53	27.9	0.6
Q47-9.1	0.46	0.00027	39.821	7030	72	0.011	28.300	0.0435	3.98	0.0280	4.58	0.0047	2.27	0.49	30.0	0.7
Q47-10.1	0.05	0.00003	49.692	1820	460	0.253	145.153	0.0567	0.70	0.6655	0.77	0.0851	0.32	0.42	526.7	1.6
Q47-11.1	0.03	0.00002	14.668	2190	26	0.012	150.719	0.0569	0.58	0.5760	0.69	0.0735	0.36	0.53	457.0	1.6
Q47-12.1	0.02	0.00001	20.788	4731	72	0.015	364.708	0.0562	0.37	0.6385	0.60	0.0823	0.48	0.79	510.0	2.3
Q56																
Q56-1.1	9.57	0.00564	13.506	1994	12	0.01	7.960	0.0452	24.15	0.0261	24.26	0.0042	2.34	0.10	27.0	0.8
Q56-2.1	3.29	0.00194	35.667	1985	21	0.01	7.315	0.0445	4.69	0.0256	5.27	0.0042	2.40	0.46	26.7	0.7
Q56-3.1	0.97	0.00057	22.451	1800	24	0.01	6.529	0.0485	3.40	0.0281	4.15	0.0042	2.38	0.57	26.9	0.6
Q56-4.1	6.64	0.00392	44.341	1163	17	0.02	4.489	0.0506	18.76	0.0300	18.91	0.0043	2.40	0.13	27.0	1.1
Q56-5.1	1.18	0.00069	83.678	1324	14	0.01	4.908	0.0429	4.45	0.0253	5.07	0.0043	2.44	0.48	27.4	0.7
Q56-6.1	1.92	0.00113	30.168	1630	12	0.01	5.910	0.0473	3.46	0.0272	4.21	0.0042	2.39	0.57	26.6	0.7
Q56-7.1	1.01	0.00060	68.041	1593	14	0.01	6.021	0.0479	3.26	0.0289	4.02	0.0044	2.36	0.59	28.0	0.7
Q56-8.1	1.25	0.00074	33.345	1552	13	0.01	5.541	0.0495	4.56	0.0283	5.13	0.0041	2.36	0.46	26.4	0.6
Q56-9.1	<0.1	-	54.777	2068	20	0.01	7.644	0.0488	2.78	0.0289	3.63	0.0043	2.33	0.64	27.8	0.6
Q56-10.1	2.40	0.00142	27.755	1386	11	0.01	4.851	0.0469	7.98	0.0261	8.33	0.0040	2.38	0.29	25.6	0.6
Q56-11.1	0.38	0.00022	65.112	1918	17	0.01	7.010	0.0476	2.90	0.0278	3.72	0.0042	2.34	0.63	27.3	0.6
LN1																
LN1-1.1	1.50	0.00083	28.881	6203	33	0.01	12.251	0.0399	9.91	0.0125	10.64	0.0023	3.88	0.36	14.6	0.6
LN1-2.1	1.61	0.00089	19.032	8644	86	0.010	17.083	0.0329	10.04	0.0103	10.74	0.0023	3.80	0.35	14.6	0.6
LN1-2.2	1.24	0.00069	40.842	364	35	0.096	15.838	0.0667	10.00	0.4604	11.17	0.0501	4.97	0.45	314.9	15.3
LN1-3.1	1.34	0.00074	47.823	4234	15	0	8.833	0.0468	13.18	0.0155	13.76	0.0024	3.95	0.29	15.4	0.6
LN1-4.1	9.00	0.00498	15.058	5774	52	0.01	12.807	0.0671	20.58	0.0217	20.99	0.0023	4.13	0.20	15.1	0.6
LN1-5.1	1.12	0.00062	37.648	3044	7	0	6.474	0.0471	9.51	0.0159	10.30	0.0024	3.95	0.38	15.8	0.6
LN1-6.1	0.8	0.00044	46.396	3976	286	0.07	8.526	0.0394	9.51	0.0134	10.29	0.0025	3.93	0.38	15.9	0.6

LN1-7.1	0.61	0.00034	68.930	5738	102	0.02	12.182	0.0464	10.13	0.0157	10.87	0.0025	3.95	0.36	15.8	0.6
LN1-8.1	0.76	0.00042	40.835	5066	90	0.02	11.300	0.0472	6.29	0.0168	7.34	0.0026	3.78	0.52	16.6	0.6
LN1-9.1	9.46	0.00524	11.916	861	21	0.03	2.025	0.0686	21.16	0.0235	21.68	0.0025	4.72	0.22	16.0	0.8
LN1-10.1	2.82	0.00156	26.758	2851	39	0.01	5.890	0.0411	16.77	0.0132	17.22	0.0023	3.91	0.23	15.0	0.6
LN1-11.1	4.71	0.00261	17.185	3644	13	0	8.151	0.0375	21.09	0.0128	21.48	0.0025	4.06	0.19	16.0	0.6
LN2																
LN2-1.1	0.80	0.00045	40.843	2046	10	0.01	5.865	0.0409	7.91	0.0187	8.93	0.0033	4.15	0.46	20.9	0.8
LN2-2.1	0.91	0.00051	37.812	3272	13	0	9.728	0.0432	7.69	0.0204	8.75	0.0034	4.16	0.48	21.3	0.9
LN2-3.1	1.73	0.00096	31.505	1900	18	0.010	5.760	0.0428	12.12	0.0205	12.84	0.0035	4.25	0.33	22.1	0.9
LN2-4.1	1.21	0.00067	80.128	4637	79	0.02	14.493	0.0500	17.70	0.0224	18.12	0.0032	3.87	0.21	22.3	0.9
LN2-4.2	0.52	0.00029	31.627	200	51	0.257	27.481	0.0697	2.40	1.5294	4.75	0.1591	4.10	0.86	951.9	36.3
LN2-5.1	0.40	0.00022	21.338	6558	16	0	19.844	0.0467	3.43	0.0226	5.38	0.0035	4.15	0.77	22.6	0.9
LN2-6.1	1.19	0.00066	14.790	8595	5819	0.700	26.654	0.0405	6.67	0.0199	7.94	0.0036	4.31	0.54	23.0	1.0
LN2-6.2	0.21	0.00011	35.003	3447	866	0.251	180.135	0.0553	1.25	0.4631	5.50	0.0607	5.35	0.97	379.9	19.7
LN2-7.1	0.58	0.00032	18.697	2760	2338	0.88	8.095	0.0478	6.66	0.0224	7.89	0.0034	4.23	0.54	21.8	0.9
LN2-7.2	0.07	0.00004	40.400	830	172	0.207	88.976	0.0665	0.81	1.1437	4.13	0.1247	4.05	0.98	757.3	29.0
LN2-8.1	0.09	0.00005	64.609	4373	87	0.02	12.837	0.0477	2.70	0.0224	6.01	0.0034	5.36	0.89	22.0	1.2
LN2-9.1	1.15	0.00064	28.339	3101	43	0.01	8.921	0.0431	7.46	0.0197	8.54	0.0033	4.16	0.49	21.3	0.9
LN2-9.2	5.39	0.00299	31.672	270	27	0.098	12.652	0.0348	44.86	0.2472	45.12	0.0515	4.79	0.11	323.9	15.1

[a] ^{206}Pb and ^{206}Pb indicate the common and radiogenic portions, respectively; common Pb corrected using measured ^{204}Pb.
Foe ages younger than 1000 Ma, ^{206}Pb/^{238}U age is preferred; otherwise, ^{207}Pb/^{206}Pb age is reported.

operation parameters were described by *Hou et al*., [2009]. The uncertainties for individual analyses in Table 2 are given at 1σ, whereas the uncertainties on weighted mean ^{206}Pb/^{238}U ages in Figure 14 and the text are given at the 2σ level.

[34] Similar to zircons from the Yadong and Pulan shear zones, zircons from samples XH11-7 and XH10-1 have a core-rim texture in the CL images (Figure 12). For zircon rims with Th/U ratio <0.1, our U-Pb dating results yield a weighted mean ^{206}Pb/^{238}U age of 27.4 ± 0.4 Ma (MSWD = 0.17, for 14 analyses) for sample XH11-7 and 27.7 ± 0.7 Ma (MSWD = 0.03, for 10 analyses) for sample XH10-1 (Figure 13), which are comparable with the SHRIMP U-Pb dating of zircon for the Yadong shear zone. The apparent ^{206}Pb/^{238}U ages of zircon cores reveal an age population of 460–418 Ma in sample XH11-7 and 516–435 Ma in sample XH10-1, implying a magmatic event in the early Paleozoic.

5.3. ^{40}Ar/^{39}Ar Thermochronology

[35] We performed ^{40}Ar/^{39}Ar dating on biotite and muscovite from three mylonite samples Q25, Q42, and Q56 in the Yadong shear zone in the eastern GHC. Table 3 summarizes the ^{40}Ar/^{39}Ar analytical data from incremental heating experiments. As shown in Figure 14, ^{40}Ar/^{39}Ar dating on sample Q42 yields a plateau age of 12.3 ± 0.2 Ma (MSWD = 0.56) for muscovite, which is slightly older than the plateau age of 10.9 ± 0.6 Ma (MSWD = 1.7) for biotite. ^{40}Ar/^{39}Ar plateau ages of biotite are 12.8 ± 0.7 Ma (MSWD = 0.26) and 12.3 ± 0.5 Ma (MSWD = 1.6) for mylonitic Hb-Pl gneisses Q25 and Q56, respectively. Compared with the SHRIMP U-Pb ages of zircon (28–26 Ma) in the Yadong shear zone (Figure 11), the ^{40}Ar/^{39}Ar cooling ages of biotite and muscovite suggest the exhumation of the Yadong shear zone above the ductile-brittle transition depth at 13–11 Ma, probably accompanied by the activation of the STD in this region.

6. Discussion

6.1. Age and Deformation Conditions of Orogen-Parallel Extension

[36] Because clear field criteria is lacking, the timing of mylonitic deformation is a challenging problem. For zircons of magmatic and metamorphic origin, the U-Th-Pb closure temperature is ≥700 °C. In zircons with a core-rim structure, the core is often inherited from the early crystallization episode while overgrowth rims of zircon are commonly formed during the following high-temperature metamorphism. Accordingly, zircon rims in mylonites can be used to date high-temperature steps of the tectono-metamorphic history. The hydrothermal zircon could be formed at lower temperature [*Claoué-Long et al*., 1995; *Hoskin and Schaltegge*, 2003]. On the other hand, the change from ductile to brittle deformation should be slightly older than the ^{40}Ar/^{39}Ar cooling ages of biotite in mylonites because the closure temperature of the K-Ar system in biotite is 300 ± 50 °C [*Harrison et al*., 1985], which is lower than the temperature for the ductile/brittle transition in the crust (300–450 °C) [*Scholz*, 2002; *Passchier and Trouw*, 2005; *Viganò and Martin*, 2007]. Therefore, although metamorphic zircon could have grown during earlier metamorphism prior to the onset of ductile shearing, if the samples are free of later thermal reactivation, the U-Pb ages of metamorphic zircon rims and ^{40}Ar/^{39}Ar cooling ages of mica can bracket the absolute age

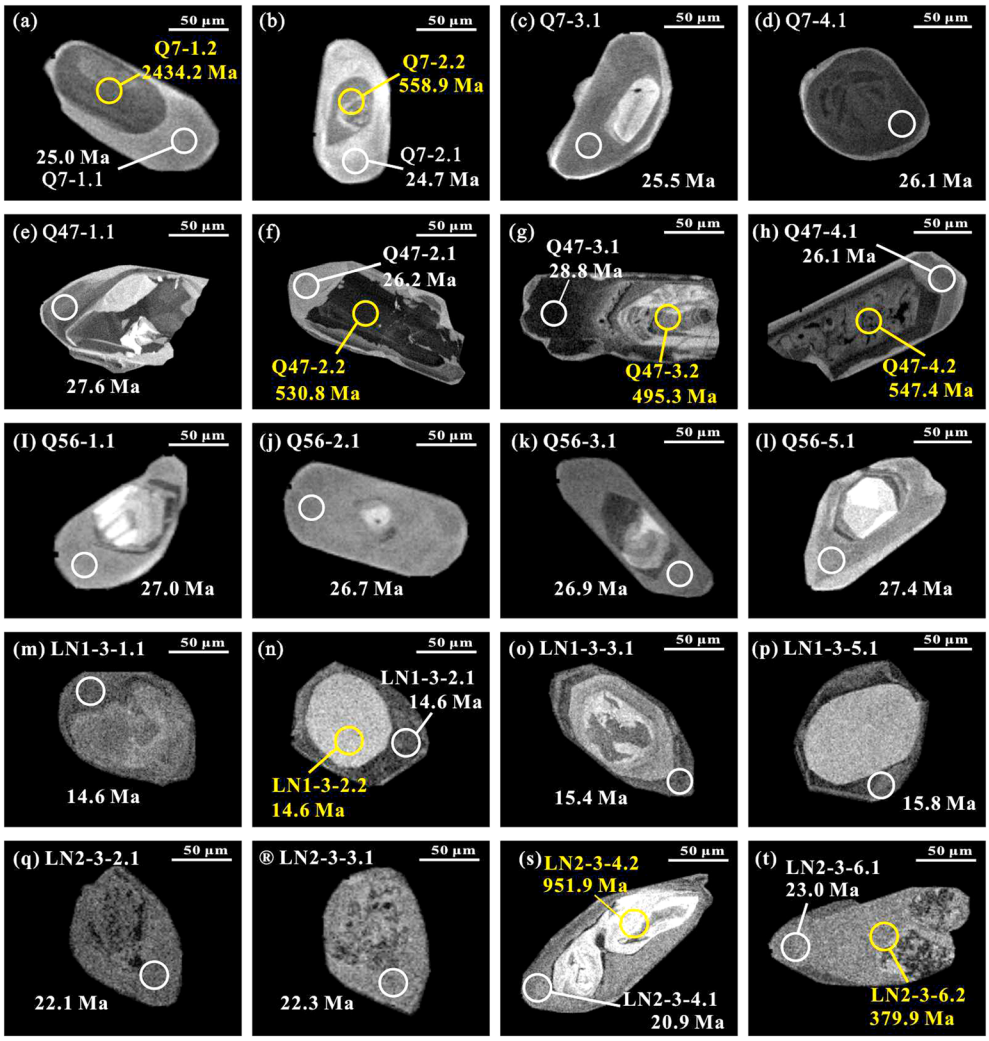

Figure 10. Cathodoluminescence images of analyzed zircon grains from Grt-Sil-Pl gneisses in the Yadong ((a–d) Q7, (e–h) Q47, and (i–l) Q56) and Pulan shear zones ((m–p) LN1 and (q–t) LN2). Circles indicate the analytical sports with a diameter of ~20 μm.

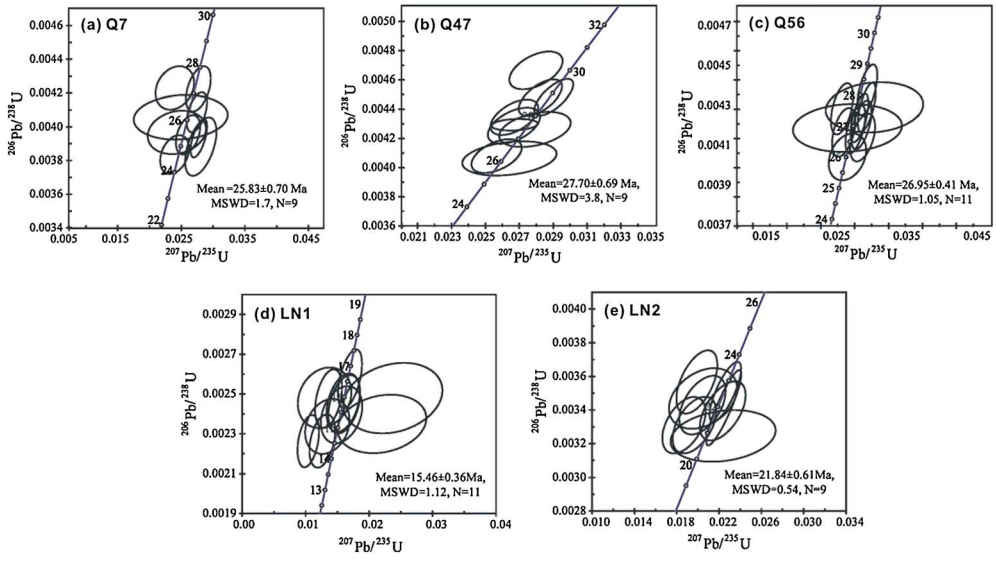

Figure 11. U-Pb concordia diagrams of zircon from Grt-Sil-Pl gneisses in the Yadong ((a) Q7, (b) Q47, and (c) Q56) and Pulan shear zones ((d) LN1 and (e) LN2) using SHRIMP analyses.

Table 2. U-Pb Data on Zircon by LA-MC-ICP-MS for Two Mylonites From the Nyalam Shear Zone

Analysis Spot	^{232}Th (ppm)	^{238}U (ppm)	^{232}Th/^{238}U	^{207}Pb/^{235}U Ratio	^{207}Pb/^{235}U $\pm1\sigma$ (%)	^{206}Pb/^{238}U Ratio	^{206}Pb/^{238}U $\pm1\sigma$ (%)	^{207}Pb/^{235}U Age (Ma)	^{207}Pb/^{235}U $\pm1\sigma$ (Ma)	^{206}Pb/^{238}U Age (Ma)	^{206}Pb/^{238}U $\pm1\sigma$ (Ma)
XH11-7											
XH11-7-1	2.91	614.06	0.005	0.0338	0.0039	0.0054	0.0004	33.7	3.8	34.7	2.4
XH11-7-2	4.19	1054.91	0.004	0.0289	0.0022	0.0042	0.0001	28.9	2.2	27	0.6
XH11-7-3	1.65	966.2	0.002	0.0287	0.0009	0.0043	0.0001	28.8	0.9	27.6	0.5
XH11-7-4	4.69	1059.86	0.004	0.0305	0.0053	0.0043	0.0002	30.5	5.3	27.6	1.5
XH11-7-5	5.67	1401.08	0.004	0.0371	0.0016	0.0042	0.0001	37	1.6	27.2	0.6
XH11-7-6	4.57	1542.57	0.003	0.0305	0.006	0.0042	0.0001	30.5	5.9	27.1	0.6
XH11-7-7	63.9	8672.65	0.007	0.0335	0.0029	0.0043	0.0003	33.5	2.9	27.8	1.8
XH11-7-8	27.99	2010.84	0.014	0.0287	0.0009	0.0043	0.0001	28.7	0.9	27.7	0.5
XH11-7-9	7.31	1362.84	0.005	0.0331	0.0027	0.0043	0.0001	33	2.6	27.6	0.7
XH11-7-10	25.41	1746.11	0.015	0.0998	0.0057	0.0155	0.0008	96.6	5.2	99	4.8
XH11-7-11	2.22	866.67	0.003	0.0281	0.0016	0.0043	0.0002	28.2	1.6	27.8	1.3
XH11-7-12	13.96	2471.1	0.006	0.0305	0.0027	0.0043	0.0001	30.5	2.7	27.7	0.6
XH11-7-13	1.54	166.36	0.009	0.0277	0.0049	0.0043	0.0003	27.8	4.9	27.7	1.6
XH11-7-14	14.33	2707.64	0.005	0.0273	0.0009	0.0042	0.0001	27.3	0.9	27.1	0.7
XH11-7-15	6.37	1423.76	0.004	0.0274	0.0009	0.0043	0.0001	27.5	0.9	27.6	0.6
XH11-7-16	4.04	993.2	0.004	0.0276	0.002	0.0043	0.0002	27.7	2	27.7	1.5
XH11-7-17	377.31	1123.81	0.336	0.3786	0.0253	0.0492	0.0032	326	19	310	19.5
XH11-7-18	52.49	487.94	0.108	0.5788	0.0188	0.0697	0.0024	464	12	435	14.2
XH11-7-19	29.67	1082.31	0.027	0.509	0.0114	0.0642	0.0013	418	8	401	7.6
XH11-7-20	267.25	962.94	0.278	0.5542	0.0155	0.0698	0.0018	448	10	435	10.7
XH11-7-21	73.79	847.33	0.087	0.5689	0.0104	0.0727	0.0011	457	7	452	6.6
XH11-7-22	34.76	566.78	0.061	0.5685	0.0099	0.0743	0.001	457	6	462	5.8
XH11-7-23	49.64	449.83	0.11	0.5736	0.0095	0.0753	0.0008	460	6	468	4.5
XH10-1-1											
XH10-1-1	10.69	2374.42	0.005	0.0252	0.0033	0.0037	0.0001	25.3	3.3	23.7	0.8
XH10-1-2	19.93	322.66	0.062	0.5332	0.0289	0.07	0.0031	434	19	436	18.8
XH10-1-3	115.47	327.39	0.353	0.5523	0.0287	0.0715	0.0031	447	19	445	18.9
XH10-1-4	46.55	7427.73	0.006	0.0258	0.0011	0.0037	0.0001	25.8	1.1	23.7	0.8
XH10-1-5	113.84	609.51	0.187	0.6901	0.0388	0.0833	0.0042	533	23	516	24.7
XH10-1-6	69.72	10023.9	0.007	0.0383	0.0039	0.0037	0.0003	38.1	3.8	23.8	2
XH10-1-7	201.22	4925.16	0.041	0.0264	0.0018	0.0037	0.0002	26.5	1.8	23.9	1.1
XH10-1-8	57.3	8813.89	0.007	0.0249	0.0014	0.0036	0.0002	25	1.4	23.3	1.1
XH10-1-9	91.01	7080.24	0.013	0.0275	0.0022	0.0036	0.0002	27.5	2.2	23.4	1.4
XH10-1-10	64.15	4660.26	0.014	0.0398	0.0039	0.0037	0.0003	39.7	3.8	23.7	2.1
XH10-1-11	72.54	12021.5	0.006	0.0277	0.0019	0.0037	0.0002	27.7	1.9	23.9	1.1
XH10-1-12	109.52	9251.79	0.012	0.026	0.0045	0.0037	0.0004	26.1	4.5	23.8	2.9
XH10-1-13	169.95	15003.4	0.011	0.0314	0.0015	0.0037	0.0001	31.4	1.5	23.9	0.7

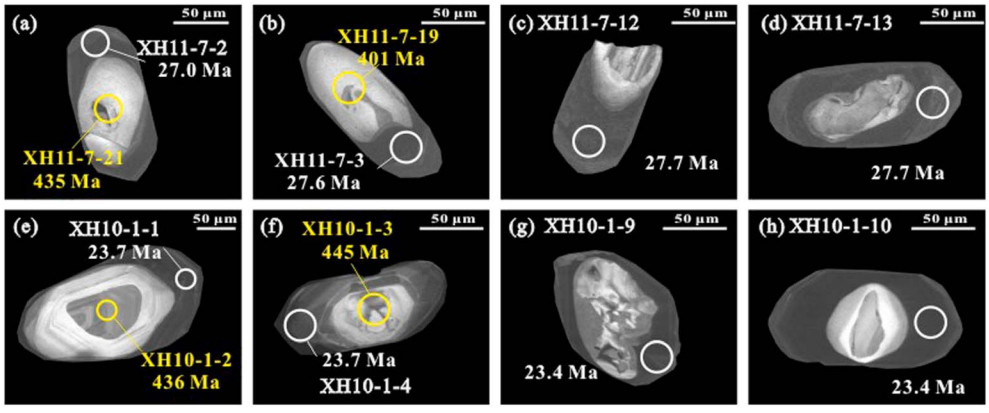

Figure 12. Cathodoluminescence images of analyzed zircon grains from Sil-Bt-Pl gneisses (a–d) XH11-7 in the Nyalam area and (e–h) XH10-1 in the Jilong area.

of deformation from high-grade to low-grade metamorphic conditions in the latest dynamothermal event.

[37] The studied zircon grains from mylonitic Grt-Sil-Pl gneisses and felsic mylonites show a core-rim structure and are free of hydrothermal alteration (Figures 10 and 12). Although the zircon cores of our samples record crystallization and metamorphism from Paleoproterozoic to early Paleozoic, the zircon rims yield very consistent ages from 15–30 Ma. The zircon rims have a homogeneous structure and Th/U ratio <0.1, suggesting that a metamorphic overgrowth of zircon occurred under the latest high-temperature episode. Meanwhile, the high-temperature *c*-slip

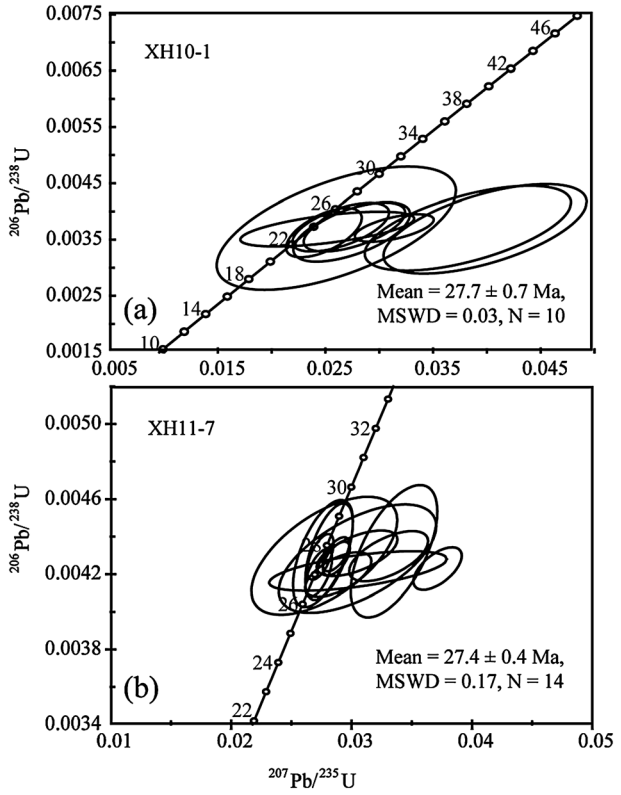

Figure 13. U-Pb concordia diagrams of zircon from Grt-Sil-Pl gneisses (a) XH10-1 and (b) XH11-7 using LA-MC-ICP-MS analyses.

and chessboard extinction of quartz, core-and-mantle structure and subgrains of plagioclase, as well as the growth of prismatic sillimanite indicate that the peak metamorphism reached upper amphibolite facies conditions (650–700 °C) during the activation of the Yadong, Nyalam, and Pulan shear zones, which are comparable with the peak metamorphic temperatures (~650–775 °C) in the GHC [e.g., *Law et al*., 2004, *Jessup et al*., 2008; *Corrie and Kohn*, 2011]. It means that even if we cannot preclude earlier equilibration, the closure of the U-Th-Pb system in the studied zircon most probably occurred during the high-temperature mylonitization.

[38] Significant crustal thickening had occurred along the length of the proto-Himalayan arc by the middle Eocene (>44 Ma) [*Aikman et al*., 2008] and in southern Tibet in the middle to late Eocene (45–30 Ma) [*Chung et al*., 2009]. The initiation age of grabens has been constrained to be 47–38 Ma by the widespread N-S trending dikes in central Tibet [*Wang et al*., 2010]. Previous estimates for the timing of prograde medium-pressure granulite facies metamorphism in the western and central Himalaya is 45–23 Ma [e.g., *Searle et al*., 1992; *Hodges et al*., 1994; *Vance and Harris*, 1999], followed by retrograde metamorphism in the early to middle Miocene (23–14 Ma) under amphibolites facies conditions [e.g., *Searle et al*., 1992; *Walker et al*., 1999]. It is expected that under crustal thickening and N-S India-Asia convergence, the middle crustal materials would flow normal to the maximum stress (vertical flattening) and develop an orogen-parallel stretching lineation. Therefore, the U-Pb ages of zircon rims of our samples fix an old limit for the age of the mylonitization and more probably date initiation of orogen-parallel ductile extension under upper amphibolite facies conditions. This event corresponds to the transition from burial/crustal thickening to exhumation in the GHC.

[39] For the Yadong shear zone in the eastern Himalaya, the SHRIMP U-Pb ages of zircon rims yield 28–26 Ma for high-temperature deformation, while the $^{40}Ar/^{39}Ar$ cooling ages of biotite and muscovite indicate cessation of ductile deformation at 13–11 Ma. Compared with the previous geochronological data for the MCT and STD in the eastern Himalaya (Figure 1), the activation of the Yadong shear zone occurred earlier than the MCT and STD. Synchronous motion of the MCT, the STD, and the Yadong shear zone in the Miocene would promote fast exhumation of the Yadong shear zone to the ductile-brittle transition depth at 13–11 Ma.

[40] Similarly, the U-Pb ages of zircon rims by LA-MC-LCP-MS provide 28–27 Ma for the activation of the Nyalam shear zone under upper amphibolite facies conditions in the central GHC. We still lack $^{40}Ar/^{39}Ar$ ages of mica for the Nyalam shear zone. $^{40}Ar/^{39}Ar$ dating on muscovite and biotite from mylonites within the STD and from its footwall in the Jilong area recorded a rapid exhumation of the GHC in the middle Miocene (16–15 Ma) [*Wang et al*., 2006]. In addition, the age of deformed leucogranites in the STD footwall is ~17 Ma in the Nyalam area [*Schärer et al*., 1986; *Xu*, 1990]. Therefore, the Nyalam shear zone probably started motion simultaneously with the Yadong shear zone, and the east-west shearing also continued to the middle Miocene during motion on the STD.

[41] In the Pulan area of the western GHC, our SHRIMP U-Pb dating of zircon rims determines 21.8–15.5 Ma for top-to-the-west shearing on the Pulan shear zone. The younger age is coeval with intrusion of leucogranites in the Gurla Mandhata dome at 16 Ma [*Wang et al*., 2005]. In addition, the $^{232}Th/^{208}Pb$ ion microprobe monazite ages of 14.8–10.8 Ma for deformed leucogranites and 13.2–9.3 Ma for undeformed leucogranites, and $^{40}Ar/^{39}Ar$ ages of muscovite and biotite from the footwall rocks of the Pulan shear zone indicate that the metamorphic rocks cooled below 400 °C at ~9 Ma [*Murphy et al*., 2002]. Clearly, the SHRIMP U-Pb ages of zircon rims at 21.8 Ma are too old to be related to the STD or the brittle Gurla Mandhata detachment $GMDF_2$ by *Murphy et al*. [2002]. The wide range of SHRIMP U-Pb ages of zircon rims suggests a prolonged activation history of the Pulan shear zone under upper amphibolite facies conditions, which was followed by a fast exhumation to greenschist facies conditions between 15–9 Ma. The ductile Pulan shear zone ceased motion after 9 Ma, and then the STD controlled the east-west extension in this region. Compared with the Yadong shear zone in the eastern GHC and the Nyalam shear zone in the central GHC, the activation of the Pulan shear zone under upper amphibolite facies conditions not only started about 4–6 Ma later, but also prior to shearing on the STD and intrusion of leucogranites.

6.2. Possible Mechanisms of Orogen-Parallel Extension

[42] Our new field data, combined with previous observations [e.g., *Brun et al*., 1985; *Pêcher et al*., 1991; *Coleman*, 1996; *Murphy et al*., 2002; *Epard and Steck*, 2004; *Jessup et al*., 2008], demonstrate that orogen-parallel stretching and ductile shearing in the upper part of the GHC are not

Table 3. $^{40}Ar/^{39}Ar$ Step Heating Data on Muscovite and Biotite in the Yadong Shear Zone

T(°C)	$(^{40}Ar/^{39}Ar)_m$	$(^{36}Ar/^{39}Ar)_m$	$(^{37}Ar_0/^{39}Ar)_m$	$(^{38}Ar/^{39}Ar)_m$	F	^{39}Ar ($^{-14}$mol)	Apparent Age(Ma)	$\pm 2\sigma$(Ma)
Q42, Muscovite, Weight = 45.73 mg, J = 0.009246								
700	27.6865	0.0886	0	0.0222	5.41	1.4966	0.33	0.54
800	92.9493	0.3142	0.0009	0.0757	0.1	0.0953	0.4	1.18
900	31.9222	0.1079	0.0034	0.0338	0.15	0.0464	1.44	3.52
1000	1.9387	0.0042	0.0023	0.0137	35.36	0.6855	28.35	49.43
1050	2.2788	0.0051	0.0008	0.0136	33.43	0.7618	7.23	61.14
1100	1.3008	0.0019	0.0074	0.0147	56.93	0.7405	7.59	73.43
1150	1.1737	0.0015	0.0111	0.0148	63.1	0.7406	4.48	80.7
1250	0.9408	0.0007	0.0034	0.0133	78.16	0.7353	10.81	98.2
1400	2.2493	0.0074	0.1352	0.0443	3.03	0.0682	1.11	100
							Total age = 11.4 Ma, $t_p = 12.30 \pm 0.20$ Ma	
Q42, Biotite, Weight = 45.79 mg, J = 0.009323								
700	128.3664	0.434	0.0656	0.1031	0.09	0.1183	0.38	0.88
800	15.9821	0.0529	0.0053	0.0234	2.12	0.3386	2.54	6.75
850	6.128	0.0191	0.0016	0.0172	7.59	0.4654	5.75	20.02
900	2.2549	0.0052	0.0012	0.0142	32.16	0.7253	10.38	43.99
930	2.5264	0.0062	0.0008	0.0147	26.96	0.6812	7.25	60.74
960	4.2815	0.0125	0.0024	0.0158	13.33	0.5706	3.77	69.45
1010	7.9872	0.025	0.004	0.019	7.42	0.5925	1.91	73.85
1060	8.9816	0.0285	0.0074	0.0204	6.14	0.5515	1.38	77.02
1140	4.0669	0.0115	0.0058	0.0158	16.1	0.6547	4.91	88.36
1240	1.6348	0.0029	0.0086	0.0148	47.02	0.7687	4.32	98.34
1400	2.0992	0.0035	0.0299	0.0187	50.14	1.0525	0.72	100
							Total age = 10.6 Ma, $t_p = 10.85 \pm 0.56$ Ma	
Q25, Biotite, Weight = 45.57 mg, J = 0.011430								
700	53.7352	0.1751	0.0031	0.0489	3.71	1.9947	0.26	0.45
800	13.087	0.0434	0.0102	0.0243	2.08	0.2724	6.17	11.18
850	7.7876	0.025	0.002	0.019	4.91	0.3825	7.65	24.5
900	3.5118	0.0098	0.0012	0.0159	17.72	0.6223	9.74	41.45
950	2.8461	0.0076	0.0012	0.0156	21.36	0.6078	8.65	56.5
1000	2.8271	0.0074	0.003	0.0158	22.66	0.6406	5.87	66.7
1050	2.0628	0.0046	0.0048	0.0156	34.1	0.7034	3.68	73.11
1100	1.1208	0.0012	0.0021	0.0146	67.89	0.7609	6.25	83.99
1150	1.2381	0.0016	0.0025	0.0145	61.18	0.7575	4.89	92.5
1250	1.1988	0.0013	0.0025	0.0148	67.57	0.81	4.1	99.63
1400	8.2597	0.0266	0.2182	0.0738	5	0.4129	0.21	100
							Total age = 12.4 Ma, $t_p = 12.75 \pm 0.74$ Ma	
Q56, Biotite, Weight = 50.48 mg, J = 0.009527								
700	108.3808	0.3566	0	0.0882	2.78	3.0142	0.23	0.45
800	25.5373	0.0861	0.0027	0.0301	0.34	0.0862	1.21	2.79
850	7.295	0.0228	0.0008	0.0653	7.76	0.5659	4.69	11.87
900	4.3688	0.0124	0.0005	0.016	15.92	0.6956	8.03	27.42
950	3.4817	0.0093	0.0008	0.0152	21.15	0.7362	9.57	45.95
1000	6.0182	0.0181	0.0008	0.0174	11.18	0.673	4.53	54.72
1080	4.5598	0.0126	0.0036	0.0183	18.57	0.8467	3.56	61.61
1180	1.3225	0.0014	0.0016	0.014	68.99	0.9123	16.8	94.15
1260	6.7757	0.0204	0.0021	0.0178	11.17	0.7569	2.83	99.63
1400	14.4102	0.0467	0.1541	0.0531	4.3	0.619	0.19	100
							Total age = 13.2 Ma, $t_p = 12.33 \pm 0.48$ Ma	

restricted to a few localities but are probably ubiquitous all along the Himalaya (Figure 15). U-Pb zircon dating results indicate that orogen-parallel extension could have started earlier (28–26 Ma) in the eastern and central Himalaya than in the western Himalaya (~22 Ma). Nevertheless, all the described occurrences are not equivalent, and their age, deformation history, and interrelations with the STD and MCT remain debatable. Several mechanisms have been proposed to account for the orogen-parallel extension in the GHC: (1) dextral shearing along the STD linked to eastward Tibet extrusion [*Pêcher et al*., 1991], (2) strain partitioning by lateral crustal thickness gradients [*Coleman*, 1996], (3) detachment at the roofs of antiformal structures transverse to the orogen [*Murphy et al*., 2002], (4) a general flow of weak middle crustal materials within a channel bounded by the MCT and STD [*Jessup et al*., 2006], (5) arc-parallel extension due to oblique convergence between India and Asia [*McCaffrey and Nabelek*, 1998; *Styron et al*., 2011], and (6) outward radial expansion of the Himalayan orogen by a foreland propagation fault system [*Murphy et al*., 2009].

[43] Variations in lineation trends have been observed across a large segment of the Himalaya, e.g., the Cuona and Yadong areas in the eastern Himalaya, the Nyalam and Jilong areas [*Brun et al*., 1985; this study], Annapurnas and Manaslu transects [*Pêcher et al*., 1991; *Coleman*, 1996], Gangotri transect [*Pêcher and Scaillet*, 1989], and the Gurla Mandhata area in the western Himalaya [*Murphy et al*., 2002; this study] (Figure 15). In addition, the lineation of gneisses and mylonites in the GHC gradually rotates to the NE in the eastern syntaxis [*Xu et al*., 2012]. *Pêcher et al*. [1991] proposed that an apparent dextral shearing along the STD could result in progressive rotation of the original radial stretching lineation characterizing the MCT when climbing up from the MCT across the GHC. Although both top-to-

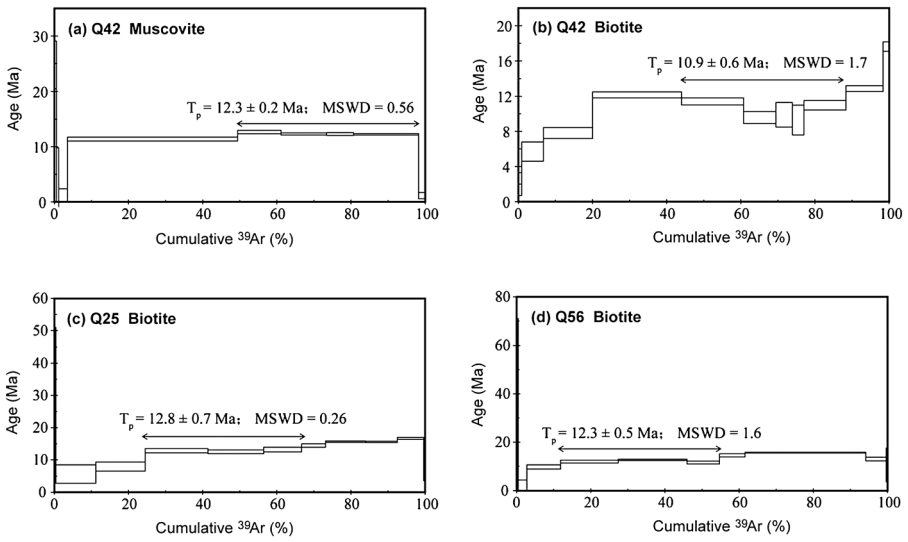

Figure 14. Ar-Ar age spectra of (a) muscovite and (b–d) biotite for mylonitic gneisses from the Yadong shear zone.

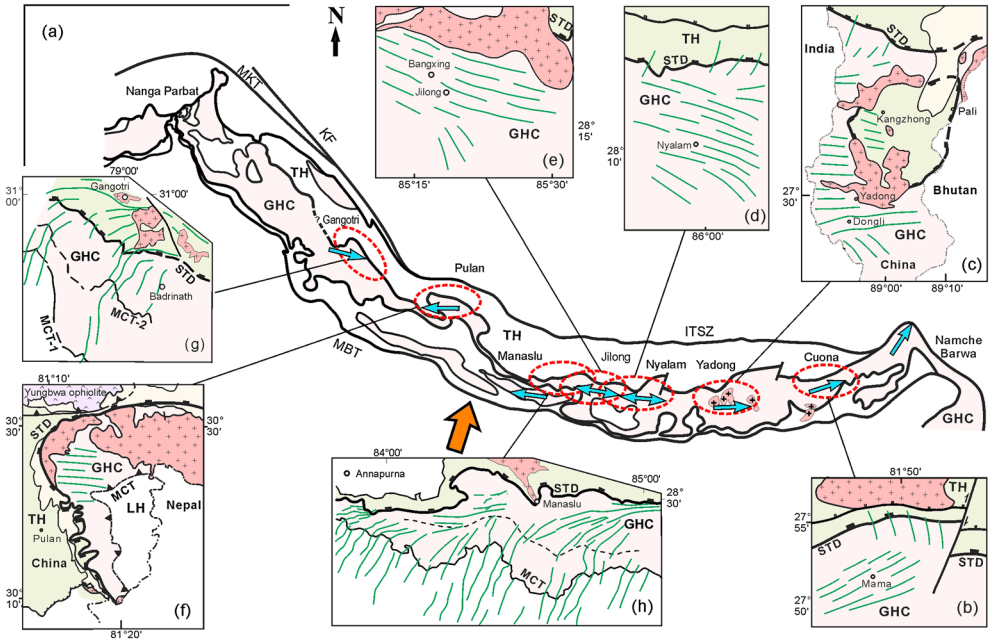

Figure 15. Stretching lineation patterns in the (a–f) studied areas, (g) the Gangotri area and (h) the Manaslu area (from [*Pêcher et al.*, 1991]). The Miocene leucogranites are shown in pink color. The red ellipses indicate areas with orogen-parallel stretching lineation in the GHC. Due to orogen-parallel gravitational collapse in the late Oligocene and Miocene, decoupling between the TH and GHC resulted in top-to-the-east shearing in the eastern Himalaya, top-to-the-west shearing in the western Himalaya, and coexistence of top-to-the-west and top-to-the-east shearing in the central Himalaya (blue arrows). The convergence direction between India and Asia is assumed to be the same as at the present (orange arrow). Abbreviations: ITSZ, Indus-Tsangbo suture zone; KF, Karakoram fault; MBT, Main Boundary Thrust; MCT, Main Central Thrust; MKT, Main Karakoram Thrust; STD, South Tibet Detachment; TH, Tethys Himalaya; GHC, Great Himalayan crystalline.

the-north shearing and strike-slip movements are superimposed in the STD in Manaslu between 25–15 Ma [*Pêcher*, 1991; *Pêcher et al.*, 1991], our field observations show that the predominant stretching lineation in the GHC changes to normal to the orogen when close to the STD (Figures 2–6), suggesting a regional north directed extension rather than a dextral slip along the STD. In addition, both top-to-the-west and top-to-the-east shear fabrics in the Nyalam shear zone required vertical flattening under a pure shear regime, rather than a strike slip under a simple

shear regime in the central GHC. Therefore, the hypothesis of dextral shearing along the STD is not favored for out data. The apparent dextral shearing along the STD in Manaslu may be caused by the coeval activation of top-to-the-west shearing and the STD in the early Miocene.

[44] *Coleman* [1996] observed coeval west-directed extension in the Marsyandi region and north-directed extension in the Dudh Khola region and attributed it to the strain partitioning in the Manaslu area by local, lateral crustal thickness gradients. Although crustal thickening did occur since the middle Eocene in the proto-Himalayan arc and in southern Tibet [*Aikman et al*., 2008; *Chung et al*., 2009], local variations in the crustal thickness in the Oligocene and Miocene are still unknown. As discussed above, the east-west stretching structures were formed earlier than the initial motion on the STD and intrusion of leucogranites. Coeval ductile orogen-perpendicular extension may have not operated until the middle Miocene. Thus, we need some other mechanisms to explain the age relationship between the two contrasting stretching structures.

[45] Detachments at the roof of the transverse domal structures deforming or cutting across the STD have been described in the GHC. For example, the Gurla Mandhata detachment system (the Pulan shear zone and the STD in this study) may account for ~20 km in exhumation and up to 60 km slip in the Gurla Mandhata dome [*Murphy et al*., 2002]. Exhumation of the Ama Drime massif in Tibet-Nepal [*Jessup et al*., 2008; *Cottle et al*., 2009; *Leloup et al*., 2010] and the Leo Pargil dome in NW India [*Thiede et al*., 2006; *Langille et al*., 2012] was kinematically linked to the orogen-parallel extension along its two bounding shear zones with opposite shear senses. In this case, the geometry is similar to that of a metamorphic core complex, while the shear sense is opposite on the two sides of the dome. Such orogen-parallel extension could produce ductile detachments at great depths but brittle normal faults at shallow structural levels and rapid exhumation of the GHC in localized regions. However, as the authors documented, the detachments only occurred at shallow depths under brittle-ductile transition conditions and probably later than the activation of the STD [*Jessup et al*., 2008; *Cottle et al*., 2009; *Langille et al*., 2012], which is contrary to the high-temperature deformation of the ductile shear zones in this study. In fact, this late doming process may facilitate erosion of the hanging wall of the shear zones and allow the final exposure of the structurally lower shear zones.

[46] Using 2-D numerical modeling, *Beaumont et al*. [2001] interpreted the Himalayan tectonics as extrusion of a low-viscosity channel within the middle crust coupled with focused surface denudation. Pervasive ductile deformation of the GHC is characterized by heterogeneous, general non-coaxial flow (components of both simple and pure shear) within the core of the GHC, with a downward increasing pure shear component toward the MCT and an increasing simple shear component toward the STD, rather than by the ideal simple shear [*Grasemann et al*. 1999; *Vannay and Grasemann*, 2001; *Jessup et al*., 2006]. The calculated kinematic vorticity of the GHC rocks demonstrates that the extrusion of the middle crust was facilitated by about 50% pure shear strain [*Larson and Godin*, 2009]. In a general flow model, the internal flow bounded by the MCT and STD will accommodate orogen-parallel stretching in the GHC, which means a predominant orogen-parallel stretching along the boundary faults with coeval orogen-parallel stretching in the core of the GHC. Clearly, this model does not take into account the along-strike changes in flow direction and does not support the initiation of orogen-parallel extension earlier than the activation of the STD either.

[47] *McCaffrey and Nabelek* [1998] proposed that the active arc-parallel extension in the Himalaya orogen can be explained by the oblique convergence between India and Asia. Oblique convergence in the east (where the strike of the belt is N80°E) will favor eastward translation of the Himalaya, frontal convergence in the central Himalaya (striking N110°E) will favor constriction, while in the west, inversion of the sign of the angle (where the strike of the belt is NW) should lead to preferential westward translation of the Himalaya. If the present India-Asia convergence direction (N20–30°E) and the arc shape of the Himalaya orogen were valid for the late Oligocene and Miocene, this model will predict widespread formation of N-S grabens (arc-perpendicular normal faults) and arc-parallel strike-slip faults in the proto-Himalaya. However, as summarized by *Styron et al*. [2011], the initiation of syncollisional brittle extension and strike-slip faulting occurred after the cessation of local activity on the MCT and STD. Given the along-strike variations in crustal shortening and strike-slip faults in the two syntaxes [*Yin*, 2006], the arc shape of the Himalayan orogen might not have formed until the late Miocene. Particularly, this 2D model cannot explain the observed strain localization in the gently dipping shear zones between the GHC and TH nor the coexistence of orogen-parallel and orogen-perpendicular stretching lineations in the GHC.

[48] *Murphy et al*. [2009] found late Miocene topographic inversion in the Zada basin in southwestern Tibet and proposed that after arc-normal thickening in the early Miocene to middle Miocene (25–13 Ma), a foreland propagation fault system will accommodate outward radial expansion of the Himalayan orogen and will result in ongoing arc-parallel extension. However, their model requires activation of the MCT and STD before orogen-parallel extension, which is contrary to our observations in the Yadong, Nyalam, and Pulan ductile shear zones.

6.3. 3D Extrusion of the GHC

[49] Based on our new data and previous studies, we can distinguish three deformation phases during exhumation of the GHC: (1) initial orogen-parallel extension by decoupling from the TH under upper amphibolite facies conditions in the late Oligocene to early Miocene; (2) coeval orogen-parallel extension and southward exhumation of the GHC from upper amphibolite to greenschist facies conditions in the early to middle Miocene; (3) orogen-parallel brittle extension and strike-slip faults in the Pliocene-Neogene.

[50] Here we propose a 3D extrusion of the GHC since the late Oligocene. As shown in Figure 15, the shear sense of the shear zones is predominant top-to-the-east (or NE) in the eastern Himalaya, but it appears both top-to-the-west and top-to-the-east in the central Himalaya, top-to-the-west in the Pulan area, and top-to-the-east in the Gangotri area. Given a thickened crust in the Oligocene, this deformation pattern implies the thickest crust or highest topography in the central Himalaya and east-west gravitational collapse due to the regional crustal thickness gradient. Crustal

thickening has occurred in southern Tibet and the proto-Himalaya in the middle to late Eocene, as evidenced by the simultaneous intrusion of adakites and N-S trending dikes in central Tibet [*Aikman et al*., 2008; *Chung et al*., 2009]. It is very probable that plate margin-normal convergence between India and Asia in the central Himalaya produced the thickest crust and the highest topography in the late Oligocene.

[51] The lateral pressure gradient will drive the mechanical decoupling between rheologically contrasting layers, i.e., the ductile GHC basement in the middle crust and the overlying sedimentary cover. The Yadong shear zone in the eastern Himalaya provides a good example of this decoupling process (Figure 4). In the central and western Himalaya, the lateral pressure gradient was probably irregular and smaller, and N-S compression was strong. The weak GHC rocks could flow in either direction in a bulk vertical flattening regime. This east-west extension would result in significant tectonic denudation, and then trigger and accompany with the partial melting of the middle crust and southward extrusion of the GHC between the MCT and STD. Therefore, the age of orogen-parallel stretching structures marks the transition from the regional burial/crustal thickening to exhumation.

[52] Coeval orogen-parallel extension and southward exhumation of the GHC suggest that tectonic denudation (gravitational collapse by lateral crustal thickness gradients) could be an important driving force of southward channel flow, beside focused surface denudation in the front of the Himalaya [*Beaumont et al*., 2001]. Such a 3-D tectonic model easily explains the pervasive stretching deformation in the upper part of the GHC and satisfies structural and geochronological data. However, it raises some challenging questions. First, although the U-Pb ages of metamorphic zircon rims suggest an earlier activation of the Yadong and Nyalam shear zones than the Pulan shear zone, the mechanism for the lag of the lateral flow in the western Himalaya is not clear. Second, it is still unknown where and why orogen-parallel gravitational collapse stopped in the late Miocene. In the Gangotri area of the western Himalaya, top-to-the-east shearing is observed in the GHC. Because this region is located to the west of the Karakoram fault, the Karakoram fault cannot be the western boundary of orogen-parallel extension. Intrusion of the western syntaxis in the Oligocene may be responsible for the top-to-the-east extension in this region. In addition, the GHC in northern Pakistan consists of low-grade to unmetamorphosed sedimentary strata interlayered with ~500 Ma granites, and the LH, GHC, and TH zones appear to be in stratigraphic continuity within the metamorphic hinterland [*Pogue et al*., 1999; *DiPietro and Pogue*, 2004], suggesting a different deformation history (coupling of the GHC and TH) in this region. Clearly, additional structural and geochronological data are needed to test and improve this new model. Answers to these questions will allow us to trace the material transported to the syntaxes, together with the along-strike variations in exhumation rate and erosion rate.

7. Conclusions

[53] Our new structural and geochronological data from southern Tibet demonstrate widespread lateral flow marked by orogen-parallel stretching lineation in the upper part of the GHC, which corresponds to decoupling between the high-grade GHC rocks and the overlying Tethyan Himalayan Sequence. The kinematic framework inferred from structural studies at the outcrop, together with EBSD-derived CPO of quartz from mylonites, reveals a top-to-the-east shear sense in the Yadong shear zone (eastern GHC), both top-to-the-east and top-to-the-west shearing in the Nyalam shear zone (central GHC), and a top-to-the-west shear sense in the Pulan shear zone (western GHC).

[54] Deformation of the Yadong, Nyalam, and Pulan shear zones occurred under upper amphibolite to greenschist facies conditions. The peak metamorphic temperature reached 650–700 °C during shearing. The U-Pb ages of metamorphic zircon rims probably dated the initiation of orogen-parallel ductile extension, yielding 28–26 Ma in the Yadong and Nyalam shear zones but 22–15 Ma in the Pulan shear zone. The $^{40}Ar/^{39}Ar$ cooling ages of biotite and muscovite record cessation of ductile shearing at 13–11 Ma in the Yadong shear zone and 17–16 Ma in the Nyalam shear zone. In contrast, the Pulan shear zone in the western GHC has a prolonged top-to-the-west shearing history at high temperature and was then rapidly exhumed to greenschist facies conditions before 10 Ma. Initiation of the lateral flow marks the transition from burial/crustal thickening to exhumation in the GHC.

[55] Combined with previous studies, we propose that due to the lateral crustal thickness gradients in a thickened crust, the proto-Himalaya experienced orogen-parallel gravitational collapse in the late Oligocene and Miocene. This tectonic deduction probably triggered and enhanced partial melting and southward exhumation of the GHC in the Miocene. Our new observations provide a structural framework for the 3-D modeling of tectonic evolution of the Himalaya.

[56] **Acknowledgments.** This study was supported by the National Natural Science Foundation of China (40921001) and the Geological Survey of China (1212010818094). We thank F. Roger and M. Jolivet for polishing the text; Dunyi Liu, Yusheng Wan, Jinhai Yu, and Jean-Pierre Burg for the discussion in U-Pb ages and metamorphism; Fangyuan Chen for the assistance in the EBSD measurements; and Miao Zhang for drawing the figures. We are grateful to Associate Editor Paul Kapp, Richard Law, A. Alexander G. Webb, Paul T. Robinson, and two anonymous reviewers for their constructive and detailed comments, which led to a significant improvement of this paper.

References

Aikman, A.B., T.M. Harrison, and L. Ding (2008), Evidence for early (>44 Ma) Himalayan crustal thickening, Tethyan Himalaya, southeastern Tibet, *Earth Planet. Sci. Lett.*, *274*, 14–23.

Arita, K. (1983), Origin of the inverted metamorphism of the Lower Himalayas, Central Nepal, *Tectonophysics*, *95*, 43–60.

Arita, K., R.D. Dallmeyer, and A. Takasu (1997), Tectonothermal evolution of the Lesser Himalaya, Nepal: Constraints from Ar/Ar ages from the Kathmandu Nappe, *Island Arc*, *6*, 372–385.

Beaumont, C., G.A. Jamieson, M.H. Nguy, and B. Lee (2001), Himalaya tectonics explained by extrusion of a low-viscosity crustal channel coupled to focused surface denudation, *Nature*, *414*, 738–742.

Black, L.P., et al. (2003), TEMORA 1: A new zircon standard for Phanerozoic U-Pb geochronology, *Chem. Geol.*, *200*, 155–170.

Blumenfeld, P., D. Mainprice, and J.L. Bouches (1986), C-slip in quartz from subsolidus deformed granite, *Tectonophysics*, *127*, 97–115.

Brun, J.P., J.P. Burg, and C.C. Ming (1985), Strain trajectories above the Main Central Thrust (Himalaya) in southern Tibet, *Nature*, *313*, 388–390.

Burchfiel, B.C., and L.H. Royden (1985), North–south extension within the convergent Himalayan region, *Geology*, *13*, 679–682.

Burchfiel, B.C., et al. (1992), The South Tibetan Detachment System, Himalayan orogen: Extension contemporaneous with and parallel to shortening in a collisional mountain belt, *Geol. Soc. Am. Spec. Pap.*, *269*, 1–41.

Burg, J.P., M. Brunel, D. Gapais, G.M. Chenm, and G.H. Liu (1984), Deformation of leucogranites of the crystalline main central thrust sheet in southern Tibet (China), *J. Struct. Geol.*, *6*, 535–542.

Burg, J.P., et al. (1998), The Namche Barwa syntaxis: Evidence for exhumation related to compressional crustal folding, *J. Asian Earth Sci.*, *16*, 239–252.

Carosi, R., B. Lombardo, G. Molli, G. Musumeci, and P.C. Pertusati (1998), The South Tibetan Detachment System in the Rongbuk valley, Everest region: Deformation features and geological implications, *J. Asian Earth Sci.*, *16*, 299–311.

Carosi, R., B. Lombardo, G. Musumeci, and P.C. Pertusati (1999), Geology of the Higher Himalayan crystallines in Khumbu Himal (eastern Nepal), *J. Asian Earth Sci.*, *17*, 785–803.

Catlos, E.J., C.S. Dubey, T.M. Harrison, and M.A. Edwards (2004), Late Miocene movement within the Himalayan Main Central Thrust shear zone, Sikkim, north-east India, *J. Metamorphic Geol.*, *22*, 207–226.

Chambers, J., M. Caddick, T. Argles, M. Horstwood, S. Sherlock, N. Harris, R. Parrish, and T. Ahmad (2009), Empirical constraints on extrusion mechanisms from the upper margin of an exhumed high-grade orogenic core, Sutlej valley, NW India, *Tectonophysics*, *477*, 77–92.

Chemenda, A.I., M. Mattauer, J. Malavieille, and A.N. Bokun (1995), A mechanism for syn-collisional rock exhumation and associated normal faulting—Results from physical modeling, *Earth Planet. Sci. Lett.*, *132*, 225–232.

Chemenda, A.I., J.P. Burg, and M. Mattauer (2000), Evolution model of the Himalaya–Tibet system: Geopoem based on new modeling, geological and geophysical data, *Earth Planet. Sci. Lett.*, *174*, 397–409.

Cheng, J., and G. Xu (1987), Geologic map of the Gerdake region at a scale of 1:1,000,000 and geologic report [in Chinese] p. 363, scale 1:1,000,000, Xizang Bureau of Geology and Mineral Resources, Geological Publishing House, Beijing.

Chung, S.L., et al. 2009, The nature and timing of crustal thickening in southern Tibet: Geochemical and zircon Hf isotopic constraints from postcollisional adakites, *Tectonophysics*, *477*, 36–48.

Claoué-Long, J.G., W. Compston, J. Roberts, and C.M. Fanning (1995), Two carboniferous ages: A comparison of SHRIMP zircon dating with conventional zircon ages and $^{40}Ar/^{39}Ar$ analysis, in Geochronology, Time Scale and Global Stratigraphic Correlation, edited by W.A. Berggren, D.V. Kent, M.-P. Aubry, and J. Hardenbol, pp. 3–21, SEPM (Society for Sedimentary Geology) Special Publication, *4*, Tulsa, Oklahoma.

Coleman, M.E. (1996), Orogen-parallel and orogen-perpendicular extension in the central Nepalese Himalayas, *Geo. Soc. Am. Bull.*, *298*, 553–571.

Coleman, M.E. (1998), U-Pb constraints on Oligocene–Miocene deformation and anatexis within the central Himalaya, Marsyandi valley, Nepal, *Am. J. Sci.*, *298*, 553–571.

Corrie, S.T., and M.J. Kohn (2011), Metamorphic history of the central Himalaya, Annapurna region, Nepal, and implications for tectonic models, *GSA Bull.*, *123*, 1863–1879.

Cottle, J.M., M.J. Jessup, D.L. Newell, M.S.A. Horstwood, S.R. Noble, R.R. Parrish, D.J. Waters, and M.P. Searle (2009), Geochronology of granulitized eclogite from the Ama Drime Massif: Implications for the tectonic evolution of the South Tibetan Himalaya, *Tectonics*, *28*, TC1002, doi:10.1029/2008TC002256.

Cottle, J.M., D.J. Waters, D. Riley, O. Beyssac, and M.J. Jessup (2011), Metamorphic history of the South Tibetan Detachment System, Mt. Everest region, revealed by RSCM thermometry and phase equilibria modeling, *J. Metamorphic Geol.*, *29*, 561–582.

Crouzet, C., I. Dunkl, L. Paudel, P. Árkai, T.M. Rainer, K. Balogh, and E. Appel (2007), Temperature and age constraints on the metamorphism of the Tethyan Himalaya in Central Nepal: A multidisciplinary approach, *J. Asian Earth Sci.*, *30*, 113–130.

DeCelles, P.G., D.M. Robinson, J. Quade, T.P. Ojha, C.N. Garzione, P. Copeland, and B.N. Upreti (2001), Stratigraphy, structure and tectonic evolution of the Himalayan fold-thrust belt in western Nepal, *Tectonics*, *20*, 487–509.

Ding, L., and D. Zhong (1999), Metamorphic characteristics and geotectonic implications of the high-pressure granulites from Namche Barwa, eastern Tibet, *Sci. China*, *42*, 491–505.

Ding, L., D.L. Zhong, A. Yin, P. Kapp, and T.M. Harrison (2001), Cenozoic structural and metamorphic evolution of the eastern Himalayan syntaxis (Namche Barwa), *Earth Planet. Sci. Lett.*, *192*, 423–438.

DiPietro, J.A., and K.R. Pogue (2004), Tectonostratigraphic subdivisions of the Himalaya: A view from the west, *Tectonics*, *23*, TC5001. doi:10.1029/2003TC001554.

Edwards, M.A., and T.M. Harrison (1997), When did the roof collapse? Late Miocene north–south extension in the High Himalaya revealed by Th–Pb monazite dating of the Khula Kangri granite, *Geology*, *25*, 543–546.

Edwards, M.A., W.S.F. Kidd, J.X. Li, Y.J. Yu, and M. Clark (1996), Multistage development of the southern Tibet detachment system near Khula Kangri: New data from Gonto La, *Tectonophysics*, *260*, 1–19.

Edwards, M.A., A. Pêcher, W.S.F. Kidd, B.C. Burchfield, and L.H. Royden (1999), Southern Tibet Detachment at Khula Kangri, eastern Himalaya: A large-area, shallow detachment stretching in Bhutan? *J. Geol.*, *107*, 623–631.

Epard J.L. and A. Steck (2004), The eastern prolongation of the Zanskar shear zone (western Himalaya), *Eclogae Geol. Helv.*, *97*, 193–212.

Garzanti, E. (1999), Stratigraphy and sedimentary history of the Nepal Tethys Himalaya passive margin, *J. Asian Earth Sci.*, *17*, 805–827.

Godin, L., R.L. Brown, and S. Hanmer (1999), High strain zone in the hanging wall of the Annapurna detachment, central Nepal Himalaya, in Himalaya and Tibet: Mountain Roots to Mountain Tops, GSA Special Papers, *328*, edited by A. Macfarlane, R.B. Sorkhabi, and J. Quade, pp. 199–210, Boulder, Colorado.

Godin, L., D. Grujic, R.D. Law, and M.P. Searle (2006), Channel flow, ductile extrusion and exhumation in continental collision zones: An introduction, *Geol. Soc. Spec. Publ.*, *268*, 1–23.

Grasemann, B., H. Fritz, and J.-C. Vannay (1999), Quantitative kinematic flow analysis from the Main Central Thrust Zone (NW-Himalaya, India): Implications for a decelerating strain path and the extrusion of orogenic wedges, *J. Struct. Geol.*, *21*, 837–853.

Grujic, D., M. Casey, C. Davidson, L.S. Hollister, R. Kundig, T. Pavis, and S. Schmid (1996), Ductile extrusion of the Higher Himalayan crystalline in Bhutan: Evidence from quartz micro-fabrics, *Tectonophysics*, *260*, 21–43.

Grujic, D., L.S. Hollister, and R. Parrish (2002), Himalayan metamorphic sequence as an orogenic channel: Insight from Bhutan, *Earth Planet. Sci. Lett.*, *198*, 177–191.

Guillot, S., M. Cosca, P. Allemand, and P. Le Fort (1999), Contrasting metamorphic and geochronologic evolution along the Himalayan belt, in Himalaya and Tibet: Mountain Roots to Mountain Tops, Geol. Soc. Am. Spec. Pap., vol. *328*, edited by A. Macfarlane et al., pp. 117–128, GSA, Boulder.

Guillot, S., G. Maheo, J. de Sigoyer, K.H. Hattori, and A. Pêcher (2008), Tethyan and Indian subduction viewed from the Himalayan high- to ultrahigh-pressure metamorphic rocks, *Tectonophysics*, *451*, 225–241.

Harris, N.B.W., M. Caddick, J. Kosler, S. Goswami, D. Vance, and A.G. Tindle (2004), The pressure–temperature–time path of migmatites from the Sikkim Himalaya, *J. Metamorphic Geol.*, *22*, 249–264.

Harrison, T.M., I. Duncan, and I. McDougall (1985), Diffusion of ^{40}Ar in biotite: Temperature, pressure, and compositional effects, *Geochim Cosmochim Acta*, *49*, 2461–2468.

Harrison, T.M., F.J. Ryerson, P. Le Fort, A. Yin, O. M. Lovera, and E.J. Catlos (1997), A late Miocene-Pliocene origin for the central Himalayan inverted metamorphism, *Earth Planet. Sci. Lett.*, *146*, E1–E8.

Harrison, T.M., M. Grove, K.D. McKeegan, C.D. Coath, O. Lovera, and P. Le Fort (1999), Origin and episodic emplacement of the Manaslu intrusive complex, Central Himalaya, *J. Petrol.*, *40*, 3–19.

Henry P., X. Le Pichon, and B. Goffe (1997), Kinematic, thermal, and petrological model of the Himalayas: Constraints related to metamorphism within the underthrust Indian crust and topographic elevation, *Tectonophysics*, *273*, 31–56.

Herren, E. (1987), Zanskar shear zone: Northeast-southwest extension within the Higher Himalayas (Ladakh, India), *Geology*, *15*, 409–413.

Hodges, K.V., W.E. Hames, W.J. Olszewski, B.C. Burchfiel, L.H. Royden, and Z. Chen (1994), Thermobarometric and $^{40}Ar/^{39}Ar$ geochronologic constraints on Eohimalayan metamorphism in the Dinggye area, southern Tibet, *Contrib. Mineral. Petrol.*, *117*, 151–163.

Hodges, K.V., J.M. Hurtado, and K.X. Whipple (2001), Southward extrusion of Tibetan crust and its effect on Himalayan tectonics, *Tectonics*, *20*, 799–809.

Hodges, K.V., R.R. Parrish, and M.P. Searle (1996), Tectonic evolution of the central Annapurna Range, Nepalese Himalayas, *Tectonics*, *15*, 1264–1291.

Hodges, K.V., et al. (1992), Simultaneous Miocene extension and shortening in the Himalayan orogen, *Science*, *258*, 1446–1470.

Hoskin, P.W.O., and U. Schaltegge (2003), The composition of zircon and igneous and metamorphic petrogenesis, in Rev. Mineral. Geochem., *53*, edited by J.M. Hanchar, and P.W.O. Hoskin, pp. 27–62, Mineralogical Society of America, Washington, D.C.

Hou, K.J., Li, Y.H., and Y.Y. Tian (2009), In situ U-Pb zircon dating using laser ablation-multi ion counting-ICP-MS [in Chinese with English abstract], *Mineral Deposits*, *28*, 481–492.

Hubbard, M.S., and T.M. Harrison (1989), $^{40}Ar/^{39}Ar$ age constraints on deformation and metamorphism in the MCT zone and Tibetan slab, eastern Nepal Himalaya, *Tectonics*, *8*, 865–880.

Hurtado, J.M., K.V. Hodges, and K.X. Whipple (2001), Neotectonics of the Thakkhola graben and implications for recent activity on the south detachment fault system in the central Nepal Himalaya, *GSA Bull.*, *113*, 222–240.

Jackson, S.E., N.J. Pearson, W.L. Griffin, and E.A. Belousova (2004), The application of laser ablation-inductively coupled plasma-mass spectrometry to in situ U–Pb zircon geochronology, *Chem. Geol.*, *211*, 47–69.

Jessup, M.J., R.D. Law, M.P. Searle, and M.S. Hubbard (2006), Structural evolution and vorticity of flow during extrusion and exhumation of the Greater Himalayan slab, Mount Everest massif, Tibet/Nepal: Implications for orogen-scale flow partitioning, in Channel Flow, Ductile Extrusion and Exhumation in Continental Collision Zones, edited by R. D. Law, M. P. Searle, and L. Godin, Geol. Soc. London, Spec. Publ., vol. *268*, pp. 379–414, Bath, UK.

Jessup, M.J., D.L. Newell, J.M. Cottle, A.L. Berger, and J.A. Spotila (2008), Orogen-parallel extension and exhumation enhanced by denudation in the trans-Himalayan Arun River gorge, Ama Drime Massif, Tibet–Nepal, *Geology*, *36*, 587–590.

Johnson, M.R.W., and G. Rogers (1997), Rb–Sr ages of micas from the Kathmandu complex, central Nepalese Himalaya: Implications for the evolution of the Main Central Thrust, *J. Geol. Soc.*, *154*, 863–869.

Johnson, M.R.W., G.J.H. Oliver, R.R. Parrish, and S.P. Johnson (2001), Synthrusting metamorphism, cooling, and erosion of the Himalayan Kathmandu Complex, Nepal, *Tectonics*, *20*, 394–415.

Kellett, D. A., and D. Grujic (2012), New insight into the South Tibetan detachment system: Not a single progressive deformation, *Tectonics*, *31*, TC2007, doi:10.1029/2011TC002957.

Kellett, D.A., D. Grujic, C. Warren, J. Cottle, R. Jamieson, and T. Tenzin (2010), Metamorphic history of a syn-convergent orogen-parallel detachment: The South Tibetan detachment system, Bhutan Himalaya, *J. Metamorphic Geol.*, *28*, 785–808.

Langille, J. M., M. J. Jessup, J.M. Cottle, G. Lederer, and T. Ahmad (2012), Timing of metamorphism, melting and exhumation of the Leo Pargil dome, northwest India, *J. Metamorphic Geol.*, *30*, 769–791.

Langille, J.M., M.J. Jessup, J. M. Cottle, D. Newell, and G. Seward (2010), Kinematic evolution of the Ama Drime detachment: Insights into orogen-parallel extension and exhumation of the Ama Drime massif, Tibet-Nepal, *J. Struct. Geol.*, *32*, 900–919.

Larson, K.P. and L. Godin (2009), Kinematics of the greater Himalayan sequence, Dhaulagiri Himal: Implications for the structural framework of central Nepal, *J. Geol. Soc. London*, *166*, 25–43.

Law, R.D., M.J. Jessup, M.P. Searle, M.K. Francsis, D.J. Waters, and J.M. Cottle (2011), Telescoping of isotherms beneath the South Tibetan Detachment System, Mount Everest Massif, *J. Struct. Geol.*, *33*, 1569–1594.

Law, R.D., M.P. Searle, and R.L. Simpson (2004), Strain, deformation temperatures and vorticity of flow at the top of the Greater Himalayan Slab, Everest Massif, Tibet, *J. Geol. Soc. London*, *161*, 305–320.

Le Fort, P. (1996), Evolution of the Himalaya, in The Tectonics of Asia, edited by A. Yin, and T. M. Harrison, pp. 95–106, Cambridge University Press, New York.

Leloup, P.H., G. Mahéo, N. Arnaud, E. Kali, E. Boutonnet, D. Liu, X. Liu, and H. Li (2010), The South Tibet detachment shear zone in the Dinggye area time constraints on extrusion models of the Himalayas, *Earth Planet. Sci. Lett. 292*, 1–16.

Liu, Y., and D. Zhong (1997), Petrology of high-pressure granulites from the eastern Himalayan syntaxis, *J. Metamorphic Geol.*, *15*, 451–466.

Liu, W.C., X.Q. Wan, and D.Y. Liang (2004), New achievements and main progress in geological survey of the Gyangze and Yadong sheets, *Geol. Bull. China*, *23*, 444–450.

Liu, Y.S., et al. (2010), Continental and oceanic crust recycling-induced melt-peridotite interactions in the trans-North China orogen: U-Pb dating, Hf isotopes and trace elements in zircons from mantle xenoliths, *J. Petrol.*, *51*, 537–571.

Long, S., and N. McQuarrie (2010), Placing limits on channel flow: Insights from the Bhutan Himalaya, *Earth Planet. Sci. Lett.*, *290*, 375–390.

Ludwig, K.R. (2001), Squid 1.02: A Users Manual, Special Publication *2*, 19 pp, Berkeley Geochronology Center, Berkeley, California.

Mainprice, D., J.L. Bouchez, P. Blumenfeld, and J.M. Tubià (1986), Dominant c slip in naturally deformed quartz: Implications for dramatic plastic softening at high temperature, *Geology*, *14*, 819–822.

McCaffrey, R., and J. Nabelek (1998), Role of oblique convergence in the active deformation of the Himalayas and Southern Tibet plateau, *Geology*, *26*, 691–694.

Metcalfe, R.P. (1993), Pressure, temperature and time constraints on metamorphism across the Main Central Thrust zone and High Himalayan slab in the Garhwal Himalayai, in Himalayan Tectonics, P.J. Treloar, and M.P. Searle, edited by Geol. Soc. London, Spec. Publ., vol. *74*, pp. 485–509, Bath, UK.

Murphy, M.A. (2007), Isotopic characteristics of the Gurla Mandhata metamorphic core complex: Implications for the architecture of the Himalayan orogen, *Geology*, *35*, 983–986.

Murphy, M.A., and P. Copeland (2005), Transtensional deformation in the central Himalaya and its role in accommodating growth of the Himalayan orogen, *Tectonics*, *24*, TC4012, doi:10.1029/2004TC001659.

Murphy, M.A. and T.M. Harrison (1999), Relationship between leucogranites and the Qomolangma detachment in the Rongbuk Valley, South Tibet, *Geology*, *27*, 831–834.

Murphy, M.A., J.E. Saylor, and D. Ling (2009), Late Miocene topographic inversion in southwest Tibet based on integrated paleoelevation reconstructions and structural history, *Earth Planet. Sci. Lett.*, *282*, 1–9.

Murphy, M.A., A. Yin, P. Kapp, T.M. Harrison, C.E. Manning, F.J. Ryerson, L. Ding, and J.H. Guo (2002), Structural evolution of the Gurla Mandhata detachment system, southwest Tibet: Implications for the eastward extent of the Karakoram fault system, *Geol. Soc. Am. Spec. Pap.*, *114*, 428–447.

Nasdala, L., et al. (2008), Zircon M257—A homogeneous natural reference material for the ion microprobe U-Pb analysis of zircon, *Geostandards and Geoanalytical Res.*, *32*, 247–265.

Otani, M., and S. Wallis (2006), Quartz lattice preferred orientation patterns and static recrystallization: Natural examples from the Ryoke belt, *Japan, Geology*, *34*, 561–564.

Passchier, C.W., and R.A.J. Trouw, (2005), Microtectonics, Springer, Germany.

Pêcher, A. (1989), The metamorphism in the central Himalaya, *J. Metamorphic Geol.*, *7*, 31–41.

Pêcher, A. (1991), The contact between the Higher Himalaya crystallines and the Tibetan sedimentary series: Miocene large scale dextral shearing, *Tectonics*, *10*, 587–598.

Pêcher, A., and B. Scaillet, (1989), La structure du haut Himalaya au Garhwal, *Eclogae Geol. Helv.*, *82/2*, 655–668.

Pêcher, A., J.L. Bouchez, and P. Le Fort (1991), Miocene dextral shearing between Himalaya and Tibet, *Geology*, *19*, 683–685.

Pêcher, A., et al. (2008), Stress field evolution in the northwest Himalayan syntaxis, northern Pakistan, *Tectonics*, *27*, TC6005, doi:10.1029/2007tc002252.

Pogue, K.R., M.D. Hylland, R.S. Yeats, W.U. Khattak, and A. Hussain (1999), Stratigraphic and structural framework of Himalayan foothills, northern Pakistan, in Himalaya and Tibet: Mountain Roots to Mountain Tops, Geol. Soc. Am. Spec. Pap., vol. *328*, edited by A. Macfarlane, et al., pp. 257–274, Boulder, USA.

Robinson, D.M., P.G. DeCelles, C.N. Garzione, O.N. Pearson, T.M. Harrison, and E.J. Catlos (2003), Kinematic model for the Main Central Thrust in Nepal, *Geology*, *31*, 359–362.

Schärer, U., R.H. Xu, and C.J. Allègrge (1986), U–(Th)–Pb systematic and ages of Himalayan leucogranites, South Tibet, *Earth Planet. Sci. Lett.*, *77*, 35–48.

Scholz, C.H. (2002). The Mechanics of Earthquakes and Faulting, University Press, Cambridge.

Searle, M.P. (1999), Extensional and compressional faults in the Everest–Lhotse massif, Khumbu Himalaya, Nepal, *J. Geol. Soc. London*, *156*, 227–40.

Searle, M.P., and L. Godin (2003), The South Tibetan detachment and the Manaslu leucogranite: A structural reinterpretation and restoration of the Annapurna-Manaslu Himalaya, Nepal, *J. Geol.*, *111*, 505–523.

Searle, M.P., R.D. Law, L. Godin, K. Larson, M. J. Streule, J. M. Cottle, and M. J. Jessup (2008), Defining the Himalayan Main Central Thrust in Nepal, *J. Geol. Soc. London*, *165*, 523–534.

Searle, M.P., R.R. Parrish, K.V. Hodges, A. Hurford, M.W. Ayers, and M.J. Whitehouse (1997), Shisha Pangma leucogranite, South Tibetan Himalaya: Field relations, geochemistry, age, origin and emplacement, *J. Geol.*, *105*, 295–317.

Searle, M. P., D. J. Waters, A. J. Rex, and R. N. Wilson (1992), Pressure, temperature, and time constraints on Himalayan metamorphism from eastern Kashmir and western Zanskar, *J. Geol. Soc., London*, *149*, 753–773.

Seeber, L., and A. Pêcher, 1991, Strain partitioning along the Himalayan arc and the Nanga Parbat antiform, *Geology*, *26*, 791–794, doi:10.1030/0091-7613.

Simpson, R.L., R R. Parrish, M.P. Searle, and D.J. Waters (2000), Two episodes of monazite crystallization during metamorphism and crustal melting in the Everest region of the Nepalese Himalaya, *Geology*, *28*, 403–406.

Sláma, J., et al. (2008), Plesovice zircon—A new natural reference material for U-Pb and Hf isotopic microanalysis, *Chem. Geol.*, *249*, 1–35.

Stacey, J.S., and J.D. Kramers (1975), Approximation of terrestrial lead isotope evolution by a two-stage model, *Earth Planet. Sci. Lett.*, *28*, 207–221.

Steiger, R.H., and E. Jäger (1977), Subcommission on geochronology: Convention on the use of decay constants in geo- and cosmochronology, *Earth Planet. Sci. Lett.*, *36*, 359–362.

Stephenson, B.J., M.P. Searle, D J. Waters, and D.C. Rex (2001), Structure of the Main Central Thrust zone and extrusion of the high Himalayan deep crustal wedge, Kishtwar-Zanskar Himalaya, *J. Geol. Soc.*, *158*, 637–652.

Stipp, M., H. Stünitz, R. Heilbronner, and S.M. Schimid (2002), The eastern Tonale fault zone: A "natural laboratory" for crystal plastic deformation of quartz over a temperature range from 250 to 700 °C, *J. Strut. Geol. 24*, 1861–1884.

Streule, M.J., M.P. Searle, D.J. Waters, and M.S.A. Horstwood (2010), Metamorphism, melting, and channel flow in the Greater Himalayan Sequence and Makalu leucogranite: Constraints from thermobarometry, metamorphic modeling, and U-Pb geochronology, *Tectonics*, *29*, TC5011, doi:10.1029/2009TC002533.

Styron, R.H., M.H. Taylor, and M.A. Murphy (2011), Oblique convergence, arc-parallel extension, and the role of strike-slip faulting in the High Himalaya, *Geosphere*, *7*, 582–596.

Thiede, R.C., J.R. Arrowsmith, B. Bookhagen, M.O. McWilliams, E.R. Sobel, and M.R. Strecker (2005), From tectonically to erosionally controlled development of the Himalayan fold-and-thrust belt, *Geology*, *33*, 689–692.

Thiede, R.C., et al. (2006), Dome formation and extension in the Tethyan Himalaya, Leo Pargil, northwest India, *GSA Bull.*, *118*, 635–650.

Upreti, B.N., and P. Le Fort (1999), Lesser Himalayan crystalline nappes of Nepal: Problems of their origin, *Special Paper, GSA*, *328*, 225–238.

Vance, D., and N. Harris (1999), Timing of prograde metamorphism in the Zanskar Himalaya, *Geology*, *27*, 395–398.

Vannay, J.-C., and B. Grasemann, (2001), Himalayan inverted metamorphism and syn-convergence extension as a consequence of a general shear extrusion, *Geol. Magazine*, *138*, 253–276.

Vannay, J.C., B. Grasemann, M. Rahn, W. Frank, A. Carter, V. Baudraz, and M. Cosca (2004), Miocene to Holocene exhumation of metamorphic crustal wedges in the NW Himalaya: Evidence for tectonic extrusion coupled to fluvial erosion, *Tectonics*, *23*, TC1014, doi:10.1029/2002TC001429.

Viganò, A., and S. Martin (2007), Thermorheological model for the European Central Alps: Brittle-ductile transition and lithospheric strength, *Terra Nova*, *19*, 309–316, doi:10.1111/j.1365-3121.2007.00751.x.

Walker, J.D., M.W. Martin, S.A. Bowring, M.P. Searle, D.J. Waters, and K. V. Hodges (1999), Metamorphism, melting, and extension: Age constraints from the High Himalayan slab of southeast Zanskar and northwest Lahaul, *J. Geol.*, *107*, 473–495.

Wang, Y.C., X. Bin, Y.Q. Zhang, and Y.B. Wang (2005), U-Pb SHRIMP zircon ages of the Cuoguonongba tourmaline two-mica granite in Pulan, outhwest Tibet [in Chinese with English abstract], *Geotectonia et Metallogenia*, *29*, 517–521.

Wang, Y., Q. Li, and G.S. Qu (2006), $^{40}Ar/^{39}Ar$ thermochronological constraints on the cooling and exhumation history of the South Tibetan Detachment System, Nyalam area, southern Tibet, in Channel Flow, Ductile Extrusion and Exhumation in Continental Collision Zones, Geol. Soc. Spec. Publ., vol. *268*, edited by R. D. Law, et al., pp. 327–354.

Wang, Q., et al. (2010), Eocene north–south trending dikes in central Tibet: New constraints on the timing of east–west extension with implications for early plateau uplift? *Earth Planet. Sci. Lett.*, *298*, 205–216.

Webb, A.A.G., A.K. Schmitt, D. He, and E.L. Weigand (2011b), Structural and geochronological evidence for the leading edge of the Greater Himalayan crystalline complex in the central Nepal Himalaya, *Earth Planet. Sci. Lett.*, *304*, 483–495.

Webb, A.A.G., A. Yin, T.M. Harrison, J. Célérier, and W.P. Burgess (2007), The leading edge of the Greater Himalayan crystallines revealed in the NW Indian Himalaya: Implications for the evolution of the Himalayan Orogen, *Geology*, *35*, 955–958.

Webb, A.A.G., A. Yin, T.M. Harrison, J. Célérier, G.E. Gehrels, C.E. Manning, and M. Grove (2011a), Cenozoic tectonic history of the Himachal Himalaya (northwestern India) and its constraints on the formation mechanism of the Himalayan orogen, *Geosphere*, *7*, 1013–1061.

Williams, I.S., (1998), U–Th–Pb geochronology by ion microprobe. in Applications of Microanalytical Techniques to Understanding Mineralizing Processes. Rev. Econ. Geol. vol. 7, edited by McKibben, M.A., Shanks III, W.C., Ridley, W.I., pp. 1-35, Economic Geology Pub. Co., Littleton, USA.

Wu, C., K.D. Nelson, G. Wortman, S. Samson, Y. Yue, J. Li, W.S.F. Kidd, and M.A. Edward (1998), Yadong cross structure and South Tibetan Detachment in the east central Himalaya (89-90°E), *Tectonics*, *17*, 28–45.

Wyss, M., J. Hermann, and A. Steck (1999), Structural and metamorphic evolution of the northern Himachal Himalaya, NW India (Spiti-eastern Lahul-Parvati valley traverse), *Eclogae Geol. Helv.*, *92*, 3–44.

Xu, R.H. (1990), Age and geochemistry of granites and metamorphic rocks in south-central Xizang (Tibet). in Igneous and Metamorphic Rocks of the Tibetan Plateau. Chinese Academy of Geological Sciences, Science Press, pp. 287–302.

Xu, Z.Q., S.C. Ji, Z.H. Cai, L.S. Zeng, Q.R. Geng, and H. Cao (2012), Kinematics and dynamics of the Namche Barwa syntaxis, eastern Himalaya: Constraints from deformation, fabrics and geochronology, *Gondwana Res.*, *21*, 19–36.

Xu, Z.Q., Q. Wang, Z.M. Tang, and F.Y. Chen (2009), Fabric kinematics of ultrahigh-pressure metamorphic rocks from the main borehole of the Chinese Continental Scientific Drilling Project: Implications for continental subduction and exhumation, *Tectonophysics*, *475*, 235–250.

Xu, Z.Q., et al. (2005), Pan-African and early Paleozoic orogenic events in the Himalayan terrane: Inference from SHRIMP U-Pb zircon ages, *Acta Petrol. Sin.*, *21*, 1–12.

Yin, A. (2006), Cenozoic tectonic evolution of the Himalayan orogen as constrained by along-strike variation of structural geometry, exhumation history, and foreland sedimentation, *Earth Sci. Rev.*, *76*, 1–131.

Yin, A., C.S. Dubey, T.K. Kelty, A.A.G. Webb, T.M. Harrison, C.Y. Chou and J. Célérier (2010), Geologic correlation of the Himalayan orogen and Indian craton: Part 2. Himalaya structural geology, geochronology, and tectonic evolution of the eastern Himalaya, *GSA Bull.*, *122*, 360–395.

Yin, A., C.S. Dubey, A.A.G. Webb, T.K. Kelty, M. Grove, G.E. Gehrels, and W.P. Burgess (2010), Geologic correlation of the Himalayan orogen and Indian craton: Part 1. Structural geology, U-Pb zircon geochronology, and tectonic evolution of the Shillong Plateau and its neighboring regions in NE India, *GSA Bull.*, *122*, 336–359.

Yin, A., and T.M. Harrison (2000), Geologic evolution of the Himalayan-Tibetan orogen, *Ann. Rev. Earth Planet. Sci.*, *28*, 211–280.

Zhang, Q., and S.H. Li (1981), Magmatism and Metamorphism in Tibet [in Chinese with English abstract]. Science Press, Beijing.

Zhang, Z.M., J.L. Wang, G.C. Zhao, and C. Shi (2008), Geochronology and Precambrian tectonic evolution of the Namche Barwa complex from the eastern Himalayan syntaxis, Tibet, *Acta Petrol. Sin.*, *24*, 1477–1487.

Zhang, Z M., G.C. Zhao, M. Santosh, J.L. Wang, X. Dong, and J.G. Liou (2010), Two stages of granulite facies metamorphism in the eastern Himalayan syntaxis, south Tibet: Petrology, zircon geochronology and implications for the subduction of Neo-Tethys and the Indian continent beneath Asia, *J. Metamorphic Geol.*, *28*, 719–733.